

Low-Level Mesocyclonic Concentration by Nonaxisymmetric Transport. Part I: Supercell and Mesocyclone Evolution

BRIAN J. GAUDET

Naval Research Laboratory, Monterey, California

WILLIAM R. COTTON

Department of Atmospheric Science, Colorado State University, Fort Collins, Colorado

(Manuscript received 28 January 2003, in final form 3 October 2005)

ABSTRACT

An idealized simulation of a supercell using the Regional Atmospheric Modeling System (RAMS) was able to produce a low-level mesocyclone near the intersection of the forward- and rear-flank downdrafts. The creation of the low-level mesocyclone is similar to previous studies. After 3600 s, the low-level mesocyclone underwent a period of rapid intensification, during which its form changed from an elongated patch to a compact center. This transition was also accompanied by a sudden decrease in pressure (to 12 mb below that of the neighboring flow), and was found to occur even in the absence of nested grids.

It is shown that the stage of strong intensification does not begin aloft, as in the dynamic pipe effect, and then descend to the surface. Rather, the vortex is initiated near the surface, and then builds upward. The process is completed in 5 min, and the final vortex can be clearly distinguished from the larger-scale mesocyclone at the cloud base. The reduction of pressure can be explained as a consequence of the evacuation of mass in the horizontal convergence equation. This is in contrast to axisymmetric models of vortex intensification, which generally rely on the evacuation of mass in the vertical divergence equation. In the latter cases a positive horizontal convergence tendency is what initiates the concentrated vortex. However, nondivergent models prove that vorticity concentration can occur in the absence of any horizontal convergence. Here the concentration is associated with a negative horizontal convergence tendency.

1. Introduction

The formation of supercell tornadoes has been described as at least a three-step process (e.g., Rotunno 1986; Rasmussen et al. 1994). The first step is the formation of the parent supercell thunderstorm itself, characterized by a strong, deep, and persistent correlation (or anticorrelation) between vertical velocity and the vertical component of vorticity (henceforth vertical vorticity) within the storm (Browning and Ludlam 1962; Browning 1964; Doswell and Burgess 1993); the cause has been confirmed by observations (Barnes 1970), analysis (Rotunno 1981; Davies-Jones 1984), and numerical modeling (Schlesinger 1975; Klemp and Wil-

helmson 1978a,b; Wilhelmson and Klemp 1981; Weisman and Klemp 1982) to be the interaction of environmental horizontal vorticity and convection-produced updrafts.

Lemon and Doswell (1979) observed, however, that prior to tornadogenesis, the vertical vorticity maximum tends to migrate to the updraft–downdraft interface, and that storm updraft features actually weaken prior to tornadogenesis. Instead, a rear-flank downdraft (RFD) develops and descends to the surface, along with the vertical vorticity. The implication is that during this second step, a different vertical vorticity–generating process must be operating, one associated with downdrafts. Simulations have shown that the vertical vorticity of the “low-level mesocyclone” often exceeds that aloft (Klemp and Rotunno 1983). The downdraft can have at least three effects on the vertical vorticity. First, baroclinity along downdrafts can greatly increase low-level horizontal vorticity, and therefore

Corresponding author address: Brian J. Gaudet, Department of Electrical and Computer Engineering, University of New Mexico, MSC 01 1100, Albuquerque, NM 87131-0001.
E-mail: bgaudet@ece.unm.edu

the subsequent vertical vorticity after tilting (Klemp and Rotunno 1983; Rotunno and Klemp 1985). Second, the downdraft interface is a region of strong ∇w and can tilt horizontal vorticity to produce vertical vorticity within the downdraft (Davies-Jones and Brooks 1993; Adlerman et al. 1999). Third, the downdraft can transport vertical vorticity to the surface, a region where it is difficult to generate vorticity by tilting because of the $w = 0$ lower boundary condition (Davies-Jones 1982; Walko 1993).

The final stage, the concentration of a low-level mesocyclone, remains the least understood. Many observational studies have found it difficult to distinguish between low-level mesocyclones that produce strong tornadoes and those that do not (Blanchard and Straka 1998; Trapp 1999; Wakimoto and Cai 2000). Certainly, surface friction, and the consequent subcyclostrophic convergence, must play a key role in the formation of the actual vortex (Howells et al. 1988; Fiedler 1994; Lewellen et al. 1997; Nolan and Farrell 1999). A number of factors that facilitate tornadogenesis have been proposed: the intersection of a mesoscale boundary with a supercell (Grasso 1996; Finley 1997; Markowski et al. 1998a; Atkins et al. 1999; Rasmussen et al. 2000; Gilmore and Wicker 2002); the presence of large values of streamwise vorticity very near the surface (Markowski et al. 2002); large values of multiplied shear/buoyancy parameters (Rasmussen and Blanchard 1998); large values of streamwise vorticity very near the surface (Markowski et al. 1998b); and the presence of low lifting condensation levels (LCLs; Rasmussen and Blanchard 1998) and/or relatively warm RFDs (Markowski et al. 2002).

Since low-level mesocyclones have size and vorticity on the order of 10 km and 10^{-1} s^{-1} , respectively, whereas for tornadoes the values are 100 m and 1 s^{-1} , clearly convergent vorticity amplification must be a major part of any tornadogenesis theory. In other words, tornadogenesis from the standpoint of *vertical vorticity* must involve the coincidence of a source of vertical vorticity (e.g., the low-level mesocyclone) and horizontal convergence. So any tornadogenesis model must include horizontal convergence generation in addition to the low-level mesocyclone (Fig. 1). Horizontal convergence may be generated through the action of the vertical equation of motion (e.g., vertical suction) or the horizontal (e.g., the collision of outflow boundaries). One property of the vertically forced method is that, if it is imposed along the axis of an axisymmetric environment, it produces axisymmetric horizontal convergence. In this case, an intense vortex will be produced whenever the vertical vorticity becomes large enough.

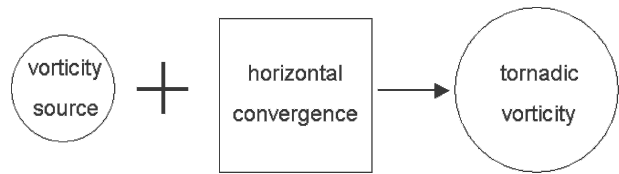


FIG. 1. Schematic depicting the evolution of tornadic vertical vorticity.

Such vortices have been produced by numerical axisymmetric fluid models with initially uniform vertical vorticity, henceforth called “tank models” for brevity (Leslie 1971; Smith and Leslie 1978; Fiedler 1994; Trapp and Davies-Jones 1997; Nolan and Farrell 1999). In these models a region of axial positive buoyancy is incorporated in the initial conditions above the surface. The buoyancy produces a toroidal circulation and low-level horizontal convergence, which amplifies the vorticity. The final steady state is one with a relative hydrostatic low underneath the positive buoyancy, with a correspondingly enhanced cyclostrophic vortex, and no further radial or vertical motion (Fiedler 1994). This state can be gradually propagated beneath the altitude of the buoyancy toward the surface in the dynamic pipe effect (DPE), or the vortex may intensify at all levels nearly simultaneously if buoyancy and/or horizontal convergence are not concentrated aloft (non-DPE vortices; see Trapp and Davies-Jones 1997; Trapp et al. 1999).

We can also attempt to examine this process from the perspective of pressure, rather than vertical vorticity, since large central pressure deficits are also a necessary result of tornadogenesis. In the buoyancy-driven tank model the presence of horizontal convergence is intimately tied to the vertical momentum equation. However, the horizontal convergence itself must be generated by horizontal radial pressure gradients. We will show how, for both DPE and non-DPE vortices, a local minimum in pressure forms in response to the divergence of the vertical momentum equation, and it is this minimum in pressure that drives the horizontal convergence. Thus, for the tank model we have the tornadogenesis picture shown in Fig. 2. The pressure decrease must lead the vorticity increase, although the lag between them may not be large. Because of the vertical coupling, the maximum tangential velocity of the tank model vortex, a function of the maximum pressure deficit, is bounded by the “thermodynamic speed limit” (Lilly 1969; Kessler 1970; Snow and Pauley 1984; Fiedler and Rotunno 1986), found by vertically integrating the buoyancy. Only in special cases can this limit be exceeded in the tank model, such as when the vortices are either supercritical or transient (Fiedler

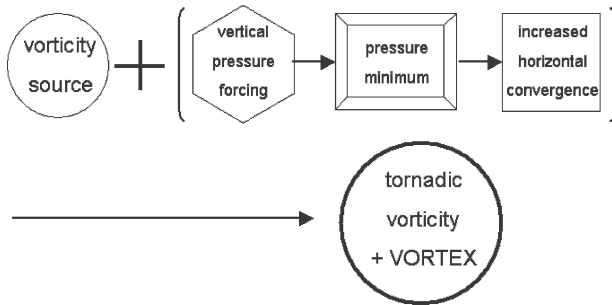


FIG. 2. Schematic depicting the typical evolution of tornadic vortex in axisymmetric vertically driven models with constant initial vorticity.

1994; i.e., precisely the cases where the vertical coupling is not active).¹

Though we have concentrated on the tank model, Fig. 2 can be applied to nonaxisymmetric models as well. Both Wicker and Wilhelmson (1995) and Grasso and Cotton (1995) modeled tornadic-strength vortices beneath idealized supercells, and suggested that they were triggered by vertical pressure gradient forces.

We now examine the case where the horizontal convergence is horizontally forced. It is possible to model this axisymmetrically, but 1) it is not likely in the atmosphere because it requires isotropic boundary conditions at infinity, and 2) if the horizontal axisymmetric forcing is not literally at infinity, parcels have the option of migrating away from the origin as well as toward it. Thus Markowski et al. (2003) showed in an axisymmetric model of tornadic convergence that increasing the intensity of an evaporatively cooled high pressure ring actually decreased convergence toward the origin. The reason is that the increased intensity entailed an increased negative buoyancy, so the inner toroidal motion was hindered, and parcels preferentially tended to infinity. So we will assume that horizontally induced horizontal convergence is nonaxisymmetric to some degree.

When nonaxisymmetric horizontal convergence is present, Fig. 1 must still represent the evolution of tornadic vertical vorticity. The key difference, however, is that Fig. 1 need not represent the evolution of *tornadic pressure*, because there is not a clear correspondence between vorticity and pressure in the nonaxisymmetric framework. For example, a strip of constant vertical vorticity with an extent in one horizontal dimension much larger than in the other (henceforth a “vorticity band”) need not be associated with any pressure deficit

even if the vertical vorticity is quite large. Such a vorticity band is often the result of strongly nonaxisymmetric convergence. We will show that large pressure deficits are associated with axisymmetric, isolated regions of vorticity with significant circulations. Thus, we will henceforth use the presence of both “large” vertical vorticity and pressure deficits as the indicator of vortexgenesis (including tornadogenesis as a specific intense case). Of course, if the horizontal convergence is nonzero, a finite-length vorticity band will become concentrated and isolated given sufficient time. However, there are also nonconvergent, horizontal advective processes that can concentrate circulation in nonaxisymmetric environments and do not require any catalyst from the vertical equation of motion.

An example of an inherently nonaxisymmetric model of tornadogenesis is that in Rotunno (1986). He proposed that a key process in the conversion of a low-level mesocyclone into a tornado was the development of a downdraft that descends on or near the low-level mesocyclone. This has been termed the “occlusion downdraft” (Klemp and Rotunno 1983), and has been seen in both models and observations as an extension of the RFD (see the review by Markowski 2002). Observations have lent support to the idea that these downdrafts are driven at least in part by near-surface low pressure associated with increased rotation (Brandes 1978; Wakimoto and Liu 1998). During the downdraft descent vertical vorticity acquires the form of a thin ring or horseshoe, which then becomes dynamically unstable and breaks down into subvortices, one of which becomes the “parent circulation” of the tornado (Rotunno 1984). Wakimoto and Liu (1998) found a similar process in observations of tornadogenesis. Rotunno (1984) numerically modeled the formation of such vortices, and Fiedler (1998) found that they could substantially exceed the thermodynamic speed limit for a finite time before being dissipated by, again, a rotationally driven downdraft.

Proof that concentrated vortices can develop through purely horizontal processes is provided by two-dimensional barotropic horizontally nondivergent models of vorticity concentration, which of course have no vertical momentum equation. The pressure in these models can be determined by a two-dimensional elliptic equation that must be satisfied if nondivergence exists. Since there is no horizontal convergence, the vertical vorticity at a point cannot increase; however, since the horizontal flux of vertical vorticity into finite-sized areas can be nonzero, the circulation within a fixed circular region can increase, indicating the development of a vortex. Kossin and Schubert (2001) modeled vorticity concentration in an idealized hurricane using a

¹ The thermodynamic speed limit also does not apply if the domain is not closed to energy fluxes (Fiedler 1994).

nondivergent model, and confirmed that the formation of a concentrated vortex central vortex was accompanied by large decreases in central pressure. That vorticity concentration is not only possible but quite frequent in two-dimensional vorticity evolution is confirmed by models of the nonlinear evolution of a vortex sheet (e.g., Rosenhead 1931; Winant and Browand 1974; Corcos and Sherman 1984), of a vortex merger (e.g., McWilliams 1984; Ritchie and Holland 1993), and of the vortex axisymmetrization (e.g., Guinn and Schubert 1993; Montgomery and Kallenbach 1997). Lee and Wilhelmson (1997a,b) applied this process to the formation of mesocyclones along a modeled outflow boundary. The evolution of tornadic-strength vortices in 2D models would follow the schematic in Fig. 3a; since the value of vertical vorticity itself cannot be changed, tornadic-valued vertical vorticity must be presupposed.

In this study we will consider models that allow 2D convergence but remain nearly 3D nondivergent. Within these models we will argue that the pressure deficits of the vortex-genesis form by two modes. The first mode is *vertically forced*, and includes both DPE and non-DPE vortices in the tank models. The pressure deficit is related to the divergence of the vertical equation of motion, which is the means of interaction with the horizontal equation of motion; the result is generally an *increased* horizontal convergence tendency (until cyclostrophy is reached). So the sequence, given by Fig. 2, has the pressure deficit as the *cause* of the concentrated vortex. The second mode is *horizontally forced*, and is a 3D analog to vortex formation in 2D models (Fig. 3b). In this mode tornadic-valued (or tornado-like vortex valued) vertical vorticity is first generated by nonaxisymmetric horizontal convergence, but is later concentrated into a vortex by horizontal advective processes similar to those in the 2D models. The presence of the vortex corresponds to a divergence in the horizontal equation of motion, which interacts with the vertical equation of motion by creating a pressure deficit. So in this case the pressure deficit is the *result* of the concentrated vortex. Also, the result of the pressure deficit is generally a *decreased* horizontal convergence tendency. Though the signs of the horizontal convergence tendencies may be counteracted by other processes, they can offer strong indications as to which vortex-genesis mode is occurring.

As an example, a three-dimensional numerical simulation is performed of an idealized supercell low-level mesocyclone using the Regional Atmospheric Modeling System (RAMS). The evolution closely resembles that of previous supercell simulations in the literature. Initially the low-level mesocyclone has the form of an

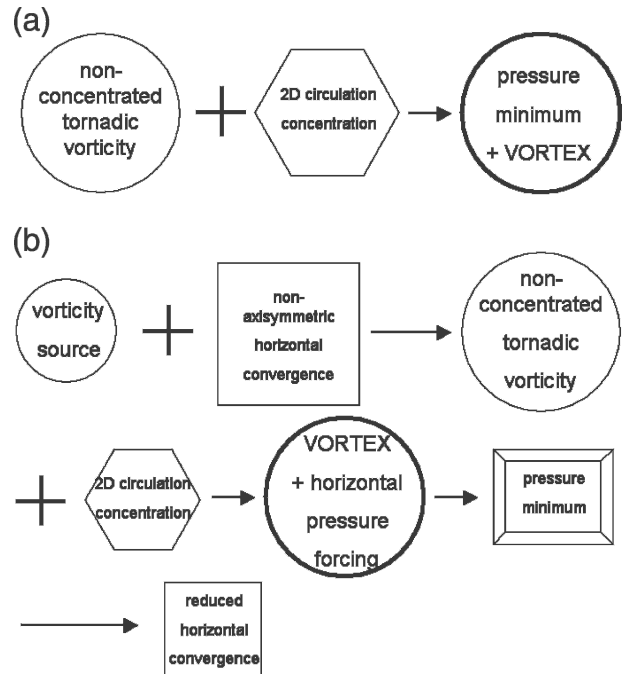


FIG. 3. Schematic depicting the typical evolution of tornadic vortex in (a) a two-dimensional horizontally nondivergent model and (b) a nonaxisymmetric, horizontally divergent horizontally driven model.

extended vorticity band along the cold pool boundary, because the horizontal convergence, while strong, is nonaxisymmetric. Soon a rapid intensification of vertical vorticity occurs within the low-level mesocyclone, accompanied by a change in vorticity morphology to an isolated vortex that migrates within the cold pool. The formation of the vortex is also associated with the formation of closed streamlines and a large decrease in pressure. We will show through both a qualitative description of the evolution and a quantitative dynamical analysis that this is an example of a three-dimensional horizontally forced vortex. We will concentrate on the period represented by the last five boxes in Fig. 3b. The decreased horizontal convergence tendency is manifested through the formation of a dynamically forced occlusion downdraft. This downdraft ultimately dissipates the vortex, but is prevented from doing so initially because the vortex tilts with height, and the cyclonic streamlines advect the downdraft away from the vortex.

2. Anelastic pressure

One form of the dry, inviscid, Boussinesq equations of motion is (Cotton and Anthes 1989):

$$\frac{d\mathbf{v}}{dt} = -\theta_{v0} \nabla \pi' + B \hat{\mathbf{k}}. \quad (1)$$

Here $\theta_{v,0}$ denotes the reference state virtual potential temperature $\theta_0(1.0 + 0.61r_{v0})$ and π is the Exner function $c_p(p/p_0)^{R/c_p}$. Each of these has been decomposed into a hydrostatic horizontally homogeneous base state, denoted by a 0 subscript, and a perturbation component, denoted by a prime superscript. The buoyant term B is given by $B = g(\theta'_v/\theta_{v,0} - r_c)$, where r_c is the condensate mixing ratio, and $\theta'_v = \theta_v - \theta_{v,0}$. The equation resembles the Boussinesq system in that horizontal variations in the density-like variable θ_v only appear in the buoyancy term. The Coriolis force has been neglected because it is not directly relevant to tornadic time and length scales.

Taking the divergence of (1) produces the (three-dimensional) divergence tendency equation. It is convenient for diagnostic purposes to put this equation into a form such that the individual terms are invariant to rotation in the x - y plane. This procedure is performed in the appendix, with the following result:

$$\frac{d}{dt}(\nabla \cdot \mathbf{v}) = -\nabla \cdot (\theta_0 \nabla \pi') + \frac{\zeta_z^2 - 3\delta^2 - \mathcal{D}^2}{2} - 2\left(\nabla_H w \cdot \frac{\partial \mathbf{v}_H}{\partial z}\right) + \frac{\partial B}{\partial z}, \quad (2)$$

where δ is the two-dimensional divergence, $(\partial u/\partial x + \partial v/\partial y)$, and \mathcal{D} is the magnitude of the horizontal deformation,

$$\mathcal{D}^2 = \left(\frac{\partial v}{\partial x} + \frac{\partial u}{\partial y}\right)^2 + \left(\frac{\partial u}{\partial x} - \frac{\partial v}{\partial y}\right)^2. \quad (3)$$

As is normally the case in the derivation, it is assumed that the three-dimensional divergence itself is so small that it can be neglected. It is possible to express this equation in a form invariant to any rotation using tensor splat and spin notation (Rotunno and Klemp 1985; Davies-Jones 2002), where spin includes the magnitude of the three-dimensional vorticity, and splat includes the effects of irrotational strain and divergence. However, because the direction of the z axis is not arbitrary but is determined by gravity, we will only use the x - y rotationally invariant form in (2).

Even with the assumption that the 3D divergence is zero, we see that 3D divergence may be created by the terms on the rhs of (2). However, the accumulation or attenuation of mass causes a change in pressure,² which

² Because of their one-to-one correspondence, “pressure” and “Exner function” will be used interchangeably in a qualitative sense within this paper.

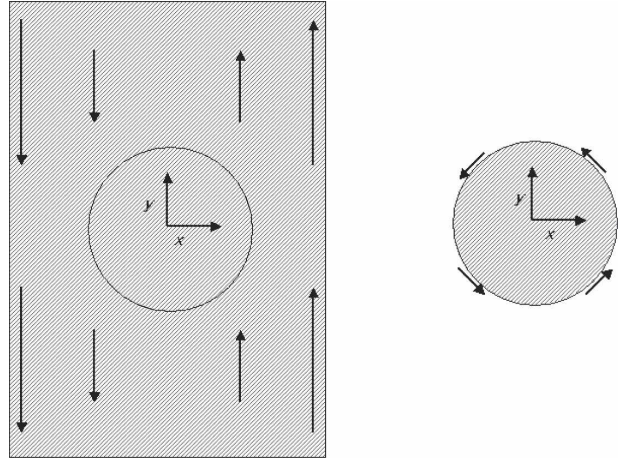


FIG. 4. Schematics depicting the vorticity band of (left) constant width, and (right) Rankine vortex. Vertical vorticity in both schematics is either zero (nonshaded) or a constant nonzero positive value (shaded). Vertical velocity and horizontal convergence are zero for both schematics. Arrows depict velocity vectors. Circles denote test contours mentioned in text.

tends to eliminate three-dimensional divergence rapidly through acoustic waves. Thus for all but the shortest time scales we may assume $\nabla \cdot \mathbf{v} \equiv 0$, which implies that the Exner function must satisfy the following:

$$\nabla \cdot (\theta_0 \nabla \pi') = \frac{\zeta_z^2 - 3\delta^2 - \mathcal{D}^2}{2} - 2\left(\nabla_H w \cdot \frac{\partial \mathbf{v}_H}{\partial z}\right) + \frac{\partial B}{\partial z}. \quad (4)$$

The unique pressure field that satisfies (4) for a region, given appropriate boundary conditions, is the anelastic pressure. If it is assumed heuristically that the π' Laplacian term is proportional but opposite in sign to π' itself (normally true for localized disturbances away from the boundaries), then positive terms on the rhs of (4) tend to create low pressure, and negative terms tend to create high pressure (Rotunno and Klemp 1982). The last term is referred to as the buoyancy forcing on π' , whereas the other terms are referred to as the dynamic forcing, and reflect the effects of advection.

The term involving vertical vorticity includes the spin contribution and is expected to lower the pressure. The deformation and divergence terms include the splat contribution, and are expected to increase the pressure. Therefore, for given vertical vorticity, the optimal wind field for reducing the pressure in a two-dimensional model ($w = 0$ and $\partial/\partial z \equiv 0$) would be one in which the deformation and divergence are zero. Now, consider Fig. 4. On the left the circular region lies within a steady-state linear shear zone, and possesses no pres-

sure variation. On the right the circular region encloses a Rankine vortex, and there is a pressure deficit at the center. Both circles are assumed to contain the same distributions of $\nabla \times \mathbf{v}_H = \zeta_{z0} \hat{\mathbf{k}} = \text{constant}$ and $\nabla \cdot \mathbf{v}_H = 0$. By Helmholtz's theorem (e.g., Batchelor 1967), the velocity distribution within each circle is completely determined by the local divergence and vorticity, and by the boundary conditions along each circle, specifically that portion of the radial velocity not attributable to the local vorticity or divergence. It follows that the deformation in a region cannot be a free parameter, but is determined by the boundary conditions of the region. In Fig. 4 we know that the shear zone has uniform deformation of ζ_{z0} (since $\mathcal{D} = \zeta = \partial v/\partial x$), whereas the Rankine vortex has no deformation within the radius of maximum winds. Evidently, for a circular patch of constant vorticity and no divergence, a radial velocity boundary condition of $v_r = 0$ is consistent with a deformation-free patch and the maximum possible pressure Laplacian (and presumably minimum possible pressure), while the first circle's boundary condition of $v_r = \zeta_{z0} r \sin(2\theta)/2$ is consistent with $\mathcal{D} = \zeta_{z0}$, which by (4) is enough to completely negate the influence of the vorticity on the pressure. The different boundary conditions along the first circle in Fig. 4 can be viewed as the net effect of all the vorticity outside of the circle. Thus, any process that advectively removes the vorticity surrounding the first circular patch (either by moving it to large distances, or incorporating it within the circular patch) can *cause* a central pressure deficit. It also follows that for a patch of uniform vorticity and convergence, the maximum pressure Laplacian occurs for a state with an *axisymmetric* radial velocity along a circular contour (because nonaxisymmetries would require the additional presence of deformation), but any such patch with uniform convergence will have a less positive pressure Laplacian than one with no convergence.

3. DPE and pressure tendencies

To clarify the dynamics of pressure reduction, we reconsider (2), but separate the vertical and horizontal momentum equations. When we also assume incompressibility, we obtain the following:

$$\begin{aligned} \frac{d}{dt} \left(\frac{\partial w}{\partial z} \right) &= - \left(\overbrace{\nabla_H w \cdot \frac{\partial \mathbf{v}_H}{\partial z}}^{\text{N}} + \delta^2 \right) - \frac{\partial}{\partial z} \left(\theta_0 \frac{\partial \pi'}{\partial z} \right) \\ &\quad + \frac{\text{V}}{\partial z} \equiv W, \end{aligned} \quad (5)$$

$$\begin{aligned} - \frac{d}{dt} \left(\frac{\partial u}{\partial x} + \frac{\partial v}{\partial y} \right) &= - \frac{\overbrace{\zeta_z^2 + \delta^2 - \mathcal{D}^2}^{\text{H}}}{2} \\ &\quad + \left(\overbrace{\nabla_H w \cdot \frac{\partial \mathbf{v}_H}{\partial z}}^{\text{N}} + \delta^2 \right) \\ &\quad + \frac{\text{PH}}{\theta_0 \nabla_H^2 \pi'} \equiv D. \end{aligned} \quad (6)$$

The horizontal Eq. (6) is found, for example, in Brandes et al. (1988) and Davies-Jones (2002). The anelastic value of π' is that which globally causes (5) and (6) to possess the same common value, which we will refer to as G . In the anelastic case $G > 0$ implies a positive horizontal convergence tendency, and $G < 0$ implies a negative horizontal convergence tendency.

If in an initially anelastic state the dynamic or buoyancy terms in (5)–(6) are modified so that $W \neq D$, the three-dimensional divergence tendency will become nonzero. In particular, if the modified W is greater (lesser) than the modified D , $\nabla \cdot \mathbf{v}$ will become positive (negative). The atmosphere's response to $\nabla \cdot \mathbf{v} > 0$ (< 0) is to decrease (increase) the pressure following the parcel. After time scales based on the speed of sound, the pressure adjusts to the anelastic pressure for the modified (5)–(6), and W and D possess a new common value, \tilde{G} .

From this description we would expect low pressure to be associated with large positive terms in (5), or large negative terms in (6). For the dynamic and buoyancy terms, we find that this relationship is the same as that in the standard heuristic application of (4). But now it can be seen that these terms can be categorized into those that evacuate mass vertically (V), those that evacuate mass horizontally (H), and those that act equally in both directions (N). The V terms are just the buoyancy terms, whereas the H terms are a subset of the dynamic terms involving horizontal motion.

Given a perturbation that causes $W > D$, the pressure rapidly changes to neutralize the three-dimensional divergence tendency and restore $W = D = \tilde{G}$. This can be accomplished by a combination of two ways; one way is to increase the term PH in (6) and thus increase D toward W . The other way is to decrease the term PV in (5) and thus decrease W toward D . As long as the decreasing pressure increases D (which will be the case if $\pi' \approx -\nabla_H^2 \pi'$), then we see that a sudden increase in the V term will not only cause a pressure decrease, but result in a new \tilde{G} greater than its initial value, G . In other words, the new anelastic state will have an increased horizontal convergence tendency.

Similarly, if decreasing the pressure decreases W (again, as expected heuristically away from boundaries), then a sudden decrease in the H term below its value in an anelastic state will result in a new $\tilde{G} < G$, and a decreased horizontal convergence tendency.

Because the proportionality between the minimum value of a function and its Laplacian at that point can be crudely estimated as the inverse square of the length scale, we can surmise that for an increased V term the new horizontal convergence tendency will be maximized if the height of the “ V signal” is much greater than its width. The reason is that for a given perturbation pressure the horizontal pressure Laplacian would far exceed the vertical one, so the increase of D toward W would far exceed the decrease of W toward D . Conversely, if an H term is made more negative, the new horizontal convergence tendency will be closest to zero (i.e., least negative) for the case of a horizontally narrow H signal. Since pressure changes for a narrow signal would affect D far more than W , the perturbed negative value of D must increase back toward W ; D would not be able to force W to decrease toward itself. Either way, horizontal convergence is most likely for vortices that show greater horizontal than vertical variation.

Admittedly a number of assumptions have been glossed over in this description [assuming that the atmosphere always relaxes to an anelastic state; assuming that functions and their Laplacians are negatively correlated, especially problematic near the surface (Davies-Jones 2002); treating the material time derivatives in (5)–(6) as if they were local time derivatives]. Thus, we should be cautious in applying this model to specific cases. We nonetheless feel that our classification can be applied to many extant models of vortex development. The non-DPE vortex of Trapp and Davies-Jones (1997) is a vortex with a vertically forced pressure core, caused by a vertical buoyancy gradient near the surface. The pressure deficit indeed induces horizontal convergence, evidently by increasing the PH term; this horizontal convergence is what spins up the vortex. Increasing vorticity leads to H becoming more negative, which tends to decrease the horizontal convergence tendency (as does the horizontal convergence itself) until a cyclostrophic state with no horizontal convergence is reached. In the DPE vortex, it is the vertical Laplacian term, PV , that serves to evacuate mass at a level, and initiates horizontal convergence. Thus both the DPE and non-DPE vortices in Trapp and Davies-Jones (1997) are vertically forced in nature.

On the other hand, vortex concentration as in the Kossin and Schubert (2001) simulation produces a horizontally forced pressure core, because the cause is $\xi_z^2 - \mathcal{D}^2$

becoming more positive (specifically, \mathcal{D} decreasing in magnitude at the nascent vortex). In three dimensions, this process would cause an increased horizontal *divergence* tendency. This indeed seems to be represented in, for example, the Klemp and Rotunno (1983) simulation, where a strengthening low-level mesocyclone dynamically induces an occlusion downdraft.

4. Numerical experiment

a. Model description

The numerical model used for these simulations is RAMS, which is described in depth in Cotton et al. (2003) and Pielke et al. (1992). RAMS is a nonhydrostatic, compressible model based on the primitive equations capable of simulating processes from the large-eddy scale to the continental scale. Predictive variables include u , v , w , the Exner function $\pi = c_p(p/p_0)^{R/c_p}$, the ice-liquid potential temperature θ_{il} (Tripoli and Cotton 1981), and various species of water substance. The variables are defined on an Arakawa C grid (Arakawa and Lamb 1981) that is either Cartesian or polar stereographic in the horizontal, and uses a terrain-following σ_z coordinate in the vertical (Gal-Chen and Somerville 1975). Two-way interactive nested grids (Clark and Farley 1984) may be spawned within any other grid. A Smagorinsky (1963) subgrid scheme is used, with the stability modifications of Lilly (1962) and Hill (1974). The microphysics scheme used in these simulations is the seven-category (cloud water, rain, pristine ice, snow, aggregates, graupel, and hail) scheme of Walko et al. (1995).

To allow the stable integration of the π and momentum tendency equations for reasonably long time steps, RAMS utilizes two methods simultaneously. First, the integration of the vertical equation is performed semi-implicitly. Second, the speed of sound is artificially reduced. The latter has not been found to make a significant difference in the solutions (Cotton and Anthes 1989). However, it can be expected that RAMS will approach an anelastic state slower than the real atmosphere. The semi-implicit approach would be expected to minimize overshoot of the anelastic solution and suppress acoustic waves.

A warm bubble (dimensions 10 km \times 10 km \times 1500 m, thermal perturbation 2 K, moisture perturbation 20%) was introduced into a horizontally homogeneous environment. The atmospheric sounding was based on that used by Grasso (2000) and van den Heever and Cotton (2004), and has been found to readily generate convection that splits into left-moving and right-moving supercells. Neither surface terrain, surface fluxes, nor radiation was operative because of the short time scales

and the desire to simplify the experiment. Furthermore, surface drag was not used in these simulations.

b. Single-grid experiment

The first simulation contains a single grid of 150×150 grid points at 333-m horizontal grid spacing, with $\Delta t = 2$ s. The intentional use of a single grid is to eliminate the influence of changing the horizontal grid spacing on the evolution of the vorticity. There were 35 vertical grid levels with spacing increasing from 40 m near the ground to a maximum of 2 km. For variables other than w , the lowest level above the surface is 19 m. Due to the tendency of convection to translate off the grid, a constant velocity of $u = 6 \text{ m s}^{-1}$, $v = 13 \text{ m s}^{-1}$ was subtracted from the hodograph at the time of initialization.

The development of the convection closely resembles that of other modeled supercells in the literature (Klemp and Wilhelmson 1978a,b; Wilhelmson and Klemp 1981; Ray et al. 1981; Grasso and Cotton 1995) and will not be described in detail here. By 2700 s the convection has split into two member storms, a right mover displaying a strong correlation between positive vertical vorticity and vertical velocity and a left mover displaying an anticorrelation; both are indicative of supercells (Doswell and Burgess 1993). The left mover then moves out of the grid domain and is not consid-

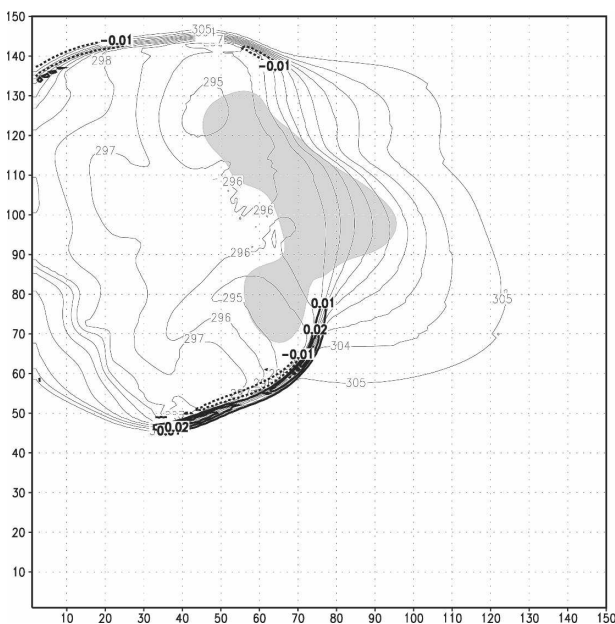


FIG. 5. Potential temperature (thin contours), vertical vorticity (thick contours), and rain mixing ratio (shaded when $>2 \text{ g kg}^{-1}$) at 2700 s and 19 m above the surface within grid 1. Contour increments are 1 K for potential temperature, 1 g kg^{-1} for the rain mixing ratio, and $1 \times 10^{-2} \text{ s}^{-1}$ for vertical vorticity.

TABLE 1. Simulation time when maximum domain vorticity becomes located at the vertically collocated vorticity center shown in the later stages of Fig. 6, for 19, 234, 608, and 1263 m above the surface.

Height	Time of jump
1263 m	3062 s
608 m	3154 s
234 m	3202 s
19 m	3222 s

ered further. A cold pool of evaporatively cooled midlevel air develops to the rear of the convection (Fig. 5), while along the forward flank there is a zone of evaporatively cooled low-level air.

The maximum vertical vorticity within the model domain at each time step after 2700 s was found for four different model levels. The heights of the four levels are 19, 234, 608, and 1263 m, and all are located beneath the mean cloud base. The location of the maximum vertical vorticity at each level versus time is shown in Table 1 and Fig. 6. Before about 3200 s, there is little spatial correlation among the four levels at a particular time. Afterward, however, the location of the maximum vertical vorticity at all the levels becomes associated with a specific horizontal location that translates to the southeast relative to the grid. This location is along the gust front, near the intersection of the warm inflow sector, the forward-flank gust front, and the rear-flank gust front, similar to the locations of the other low-level mesocyclones in the literature.

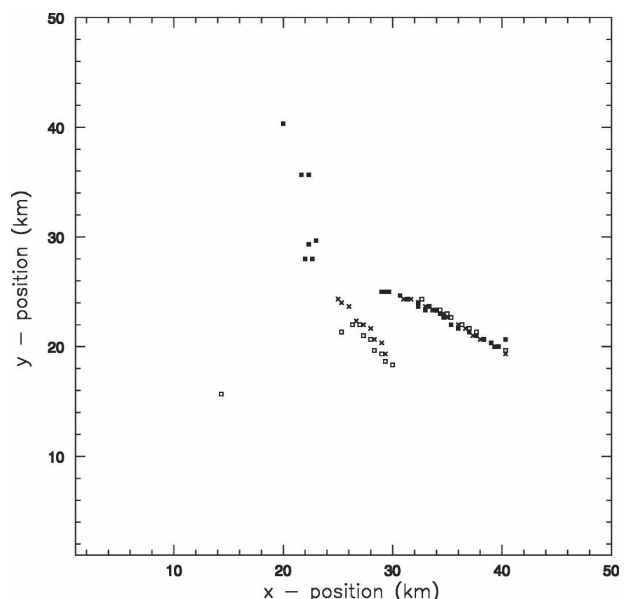


FIG. 6. Grid position of maximum domain vertical vorticity, in 50-s increments after 2700 s. The open squares: 19 m; crosses: 234 m; closed squares: 1263 m. Motion is to the east with time.

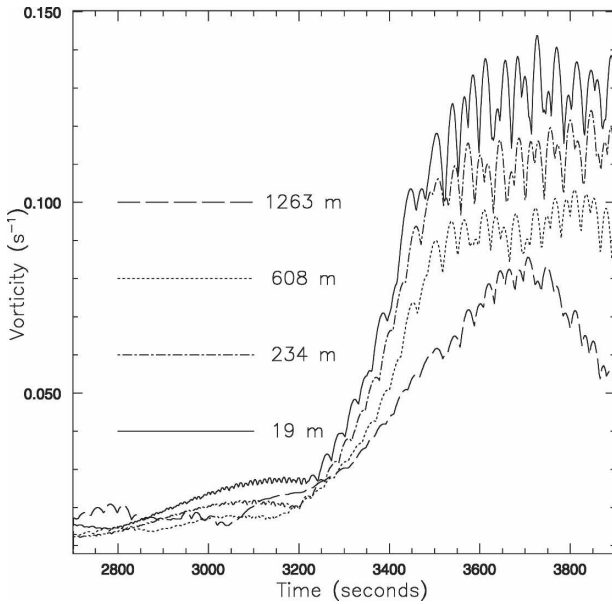


FIG. 7. Maximum vorticity within the model domain vs simulation time for 19, 234, 608, and 1263 m above the surface.

The actual values of the maximum vertical vorticity for the four levels over time are shown in Fig. 7. It can be seen that the time of the horizontal collocation of the vorticity immediately precedes a period of rapid

growth in the vertical vorticity, lasting approximately 5 min. The time period concludes with the maximum vertical vorticity (averaging 0.13 s^{-1}) occurring at the surface, nearly 5 times its value at 3200 s. (The cause of the high frequency at high vorticity values is unknown, but is associated with determining the maximum vorticity value of a translating vortex on a discrete grid.)

c. Two-grid experiment

To investigate in more detail the concentration of the vorticity, a simulation was performed in which a second grid ($\Delta x = \Delta y = 111 \text{ m}$, 119×119) was spawned after 3300 s. This time is after the vertical collocation of the vertical vorticity at all levels, but before the most rapid growth of the value of the vertical vorticity. At the initial time of the fine grid (Fig. 8) a band of vorticity is concentrated in a strip along the edge of the cold pool, approximately 1 km across. The perturbation pressure field and vortex-relative velocity vectors are shown in Fig. 9. The maximum vorticity is collocated with the maximum convergence; though convergence is large in a strip both north and south of the maximum vorticity (not shown but see wind vectors in Fig. 9 and updraft in Fig. 10), to the south (rear flank) the thermal gradient is much more intense, and this boundary will be re-

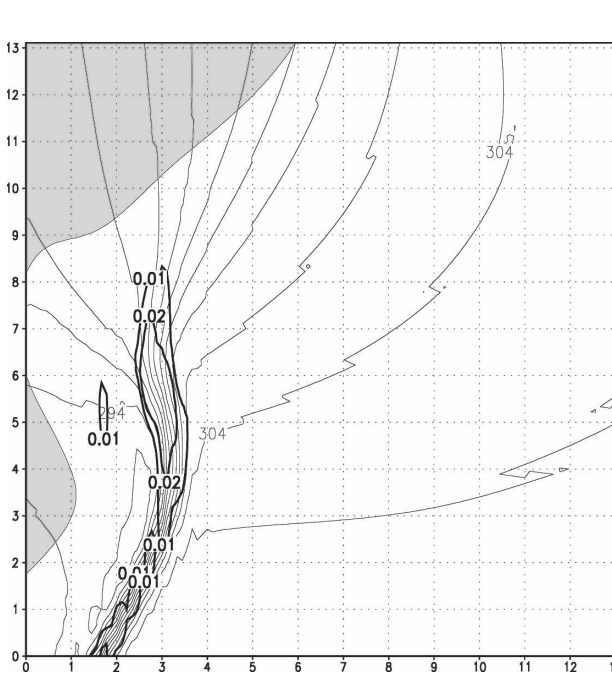


FIG. 8. Potential temperature and vertical vorticity for grid 2 at 3300 s and 19 m above the surface. Potential temperature is represented by thin contours in 1-K increments; vertical vorticity is represented by thick contours at 0.01, 0.02, and every 0.04 s^{-1} thereafter. Axes labels represent distance in km. Shading represents the rain mixing ratio $> 2 \text{ g kg}^{-1}$. The maximum vertical vorticity is 0.046 s^{-1} .

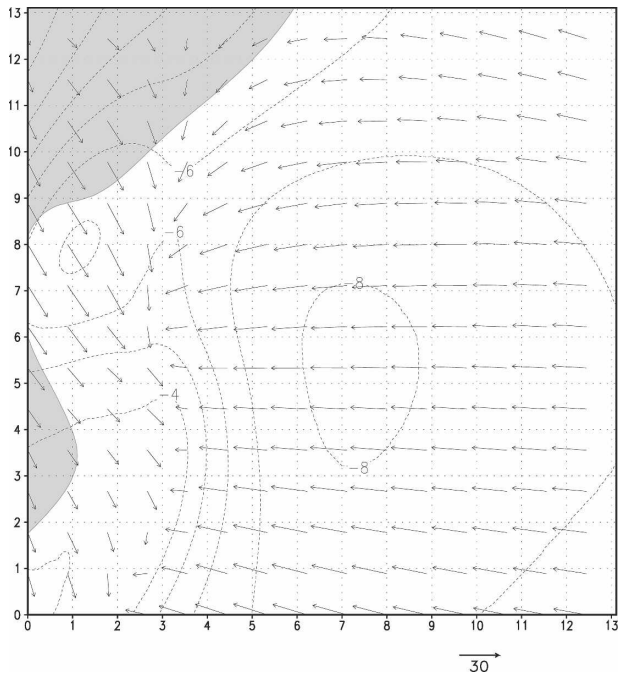


FIG. 9. Perturbation pressure and vortex-relative velocity vectors for grid 2 at 3300 s and 19 m above the surface. Contours of the perturbation pressure have an increment of 1 mb. The magnitude of the reference vector has units of m s^{-1} . Shading represents the rain mixing ratio $> 2 \text{ g kg}^{-1}$. The minimum perturbation pressure is -8.2 mb .

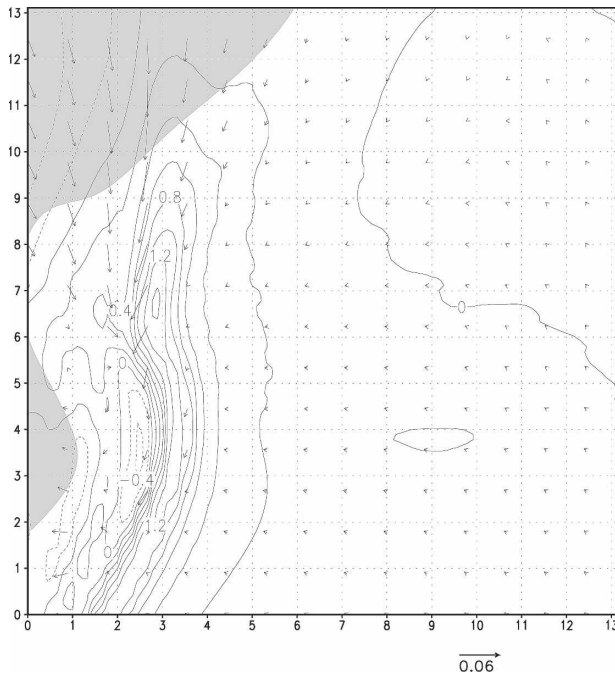


FIG. 10. Vertical velocity (thin contours) and the horizontal vorticity vectors for grid 2 at 3300 s and 19 m above the surface. Contour increment is 0.2 m s^{-1} ; negative values are dashed. The shaded region represents the rain mixing ratio $>2 \text{ g kg}^{-1}$.

ferred to as the “gust front.” No pressure deficit is apparent at the vorticity maximum; in fact, with respect to the cross-front direction, there is a relative pressure maximum in advance of the forward-flank boundary,

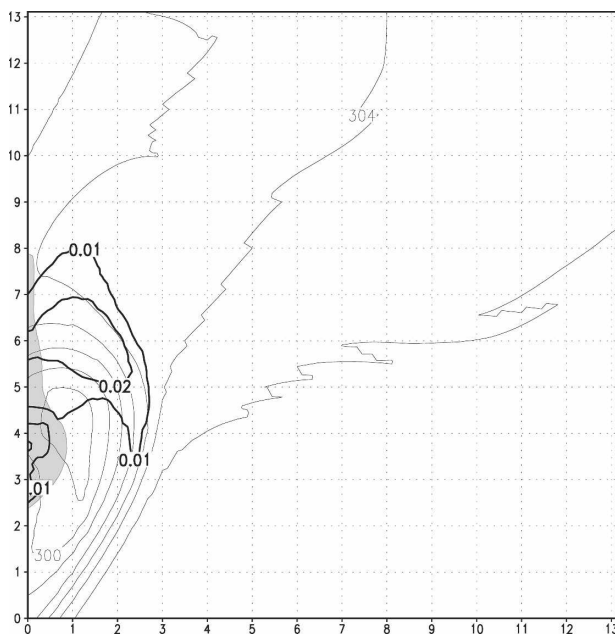


FIG. 11. Same as in Fig. 9, but at 1263 m above the surface. The minimum perturbation pressure is -11 mb .

consistent with a number of observations (Wakimoto 1982; Markowski et al. 2002). The center of the high pressure associated with the downdraft is located just to the northwest of the fine grid. There are a couple of low pressure features visible on the grid. In the surface air just east of the gust front there is a broad region of lower pressure that resembles the inflow low sometimes reported with supercell thunderstorms (Barnes 1978; Brooks et al. 1993; Rasmussen and Straka 1996; Davies-Jones 2002).

To the northwest of the vorticity maximum is another low pressure feature. This feature is most apparent near cloud base at 1263 m, and is closely associated with but slightly displaced from a rather broad region of mesocyclonic vorticity at this level (Figs. 11 and 12). At this height, the cold pool is largely absent on the forward flank, and the mesocyclone is confined to the cold pool northern periphery. Strictly speaking this is not a “divided mesocyclone” (Lemon and Doswell 1979) because the vorticity is wholly confined to updraft; however, the mesocyclone is clearly on the thermal gradient, the cool sector of which forms a notch in the updraft maximum at this level (Fig. 13).

By 3360 s (1 min later), the rapid vorticity intensification has begun (Fig. 14). The maximum vorticity in the vorticity band has now reached 0.1 s^{-1} ; this leads

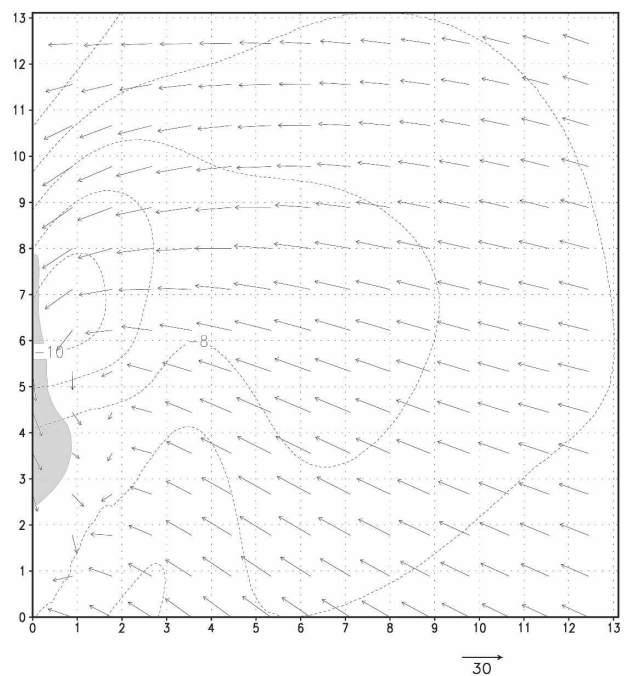


FIG. 12. Vertical velocity (thin contours) and horizontal vorticity vectors for grid 2 at 3300 s and 1263 m above the surface. The contour interval is 1 m s^{-1} ; the negative values are dashed. The shaded region represents the rain mixing ratio $>2 \text{ g kg}^{-1}$. Axes labels show the distance in km.

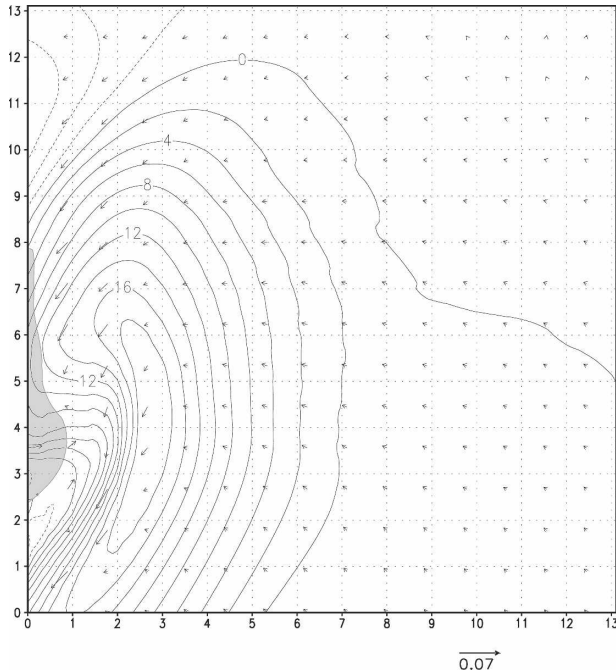


FIG. 13. Same as in Fig. 10, but at 1263 m above the surface, and with a contour increment of 1.0 m s^{-1} .

the development in the single-grid simulation by 40 s. The band itself has narrowed to approximately 400 m. There is a noticeable bowing of the line of vorticity, with a wavelength on the order of 2–3 km. The maximum vorticity occurs in the segment of the band that

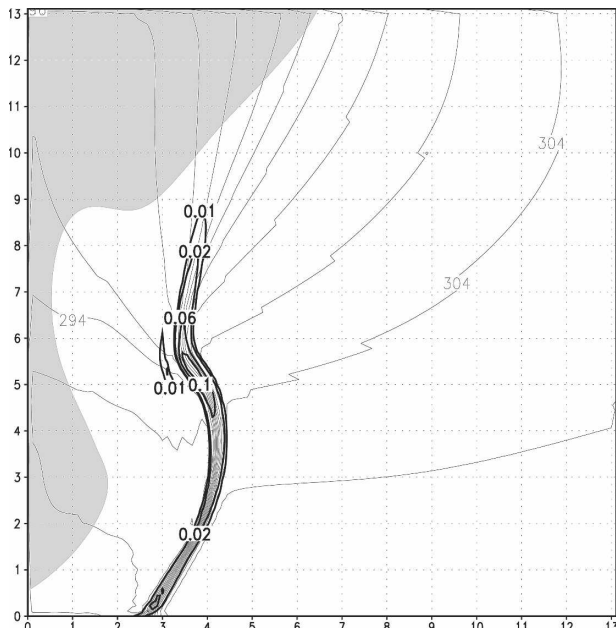


FIG. 14. Same as in Fig. 8, but at 3360 s. The maximum vertical vorticity is 0.12 s^{-1} .

has tilted into a northwest–southeast configuration. There is now a local pressure minimum at the location of the vorticity maximum (Fig. 15) that is completely absent at 1263 m (Fig. 16). A west–east cross section through the low-level vorticity maximum (Fig. 17) shows the low pressure associated with the cloud base mesocyclone and the updraft maximum along the thermal boundary, with high pressure immediately to the east. However, within the w maximum there is a zone of depressed w values, coinciding with a decrease in the pressure below 600 m.

At 3420 s (Fig. 18) the low-level vorticity has reached 0.2 s^{-1} and has become more concentrated. Vorticity trails off from the maximum in two north–south bands with an elliptical west–northwest–east–northeast core, reminiscent of vortex Rossby waves (Montgomery and Kallenbach 1997). (Some low-amplitude bands west of the thermal boundary are instances of “ringing,” due to model diffusion.) By this time a 5-mb pressure difference has developed between the new vortex and the nearby gust front (Fig. 19). Meanwhile, at 1263 m the vorticity maximum is only one-third of the surface value at this time (Fig. 20), and the pressure deficit apparent at low levels is still absent (Fig. 21). Another cross section through the low-level vorticity maximum (Fig. 22) shows an obvious pressure minimum now extending above 1000 m. The retardation of w has also

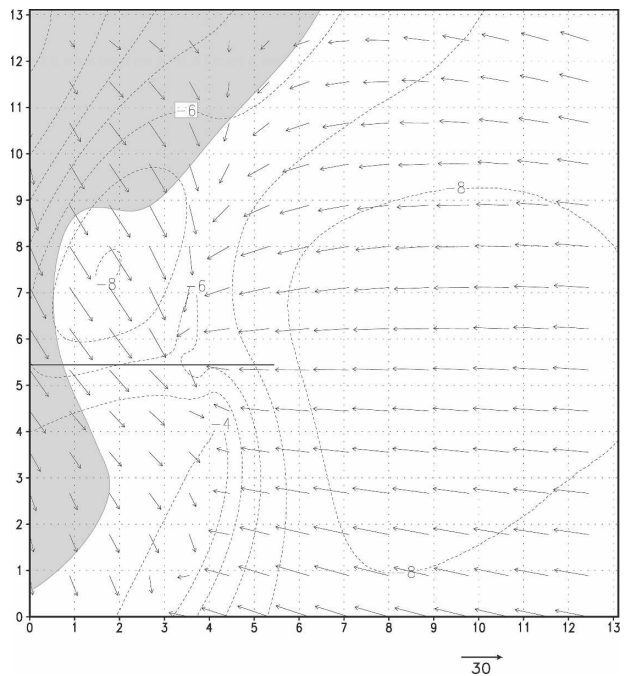


FIG. 15. Same as in Fig. 9, but at 3360 s. The minimum perturbation pressure is -8.8 mb . The solid line indicates the cross section in Fig. 17.

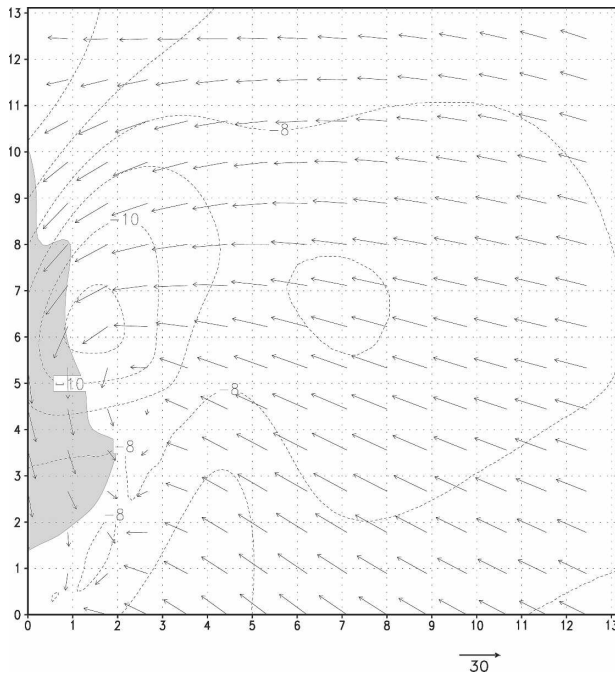


FIG. 16. Same as in Fig. 11, but at 3360 s. The minimum perturbation pressure is -11 mb.

intensified, and below 350 m, a downdraft is present. The fact that only suppression of w is apparent in the core of the pressure tube suggests that the pressure reduction initiated at the surface (or nearly simulta-

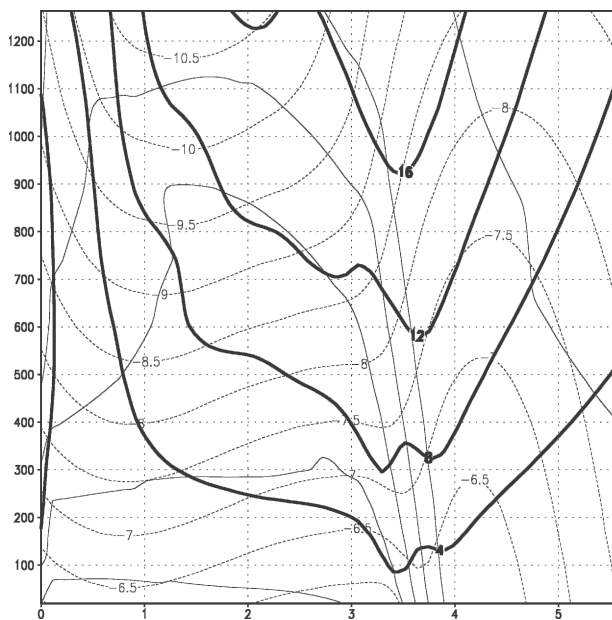


FIG. 17. West-east cross section through the vorticity maximum in Fig. 14. Thick solid contours are the vertical velocity in m s^{-1} ; thin solid contours are potential temperature; thin dashed contours are perturbation pressure in mb. Labels on the x axis are horizontal distance in km; labels on the y axis are elevation in m.

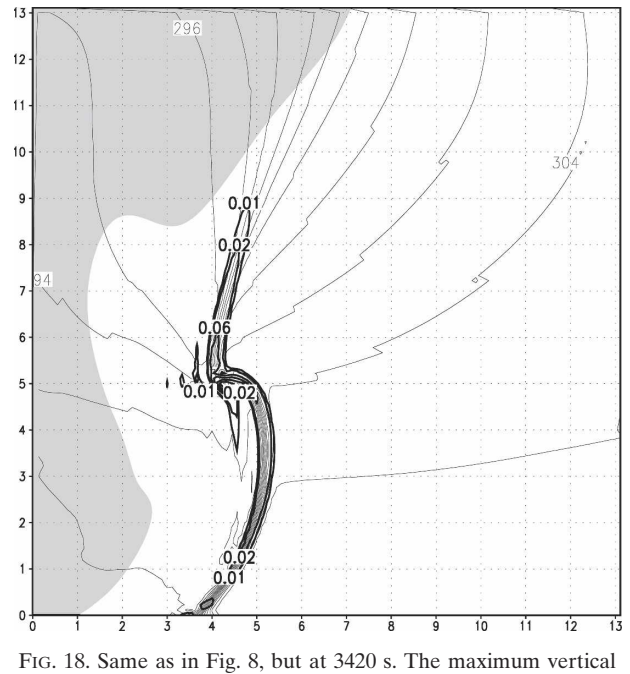


FIG. 18. Same as in Fig. 8, but at 3420 s. The maximum vertical vorticity is 0.21 s^{-1} .

neously in a layer near the surface) and built upward, rather than initiated aloft, and built downward.

By 3600 s, the surface vortex is near its peak (Fig. 23). The maximum vorticity has concentrated into a circular region that has migrated to the southwest away from

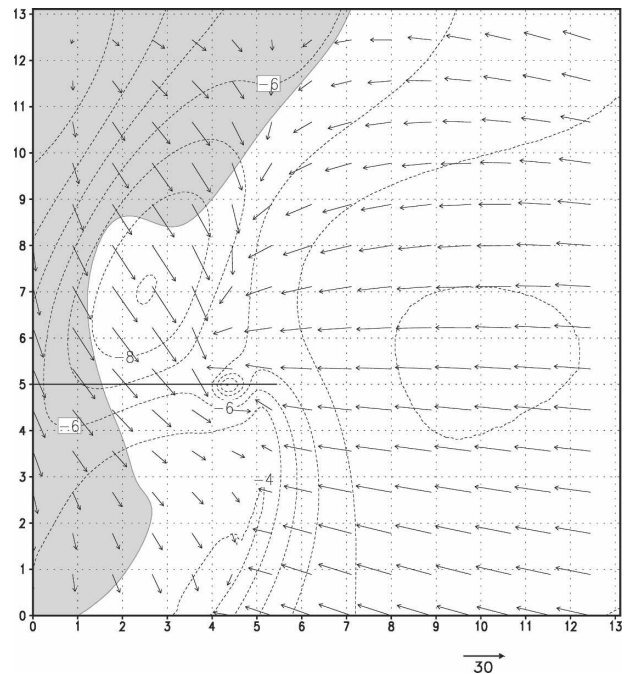


FIG. 19. Same as in Fig. 9, but at 3420 s. The minimum perturbation pressure is -10 mb. The solid line indicates the cross section in Fig. 22.

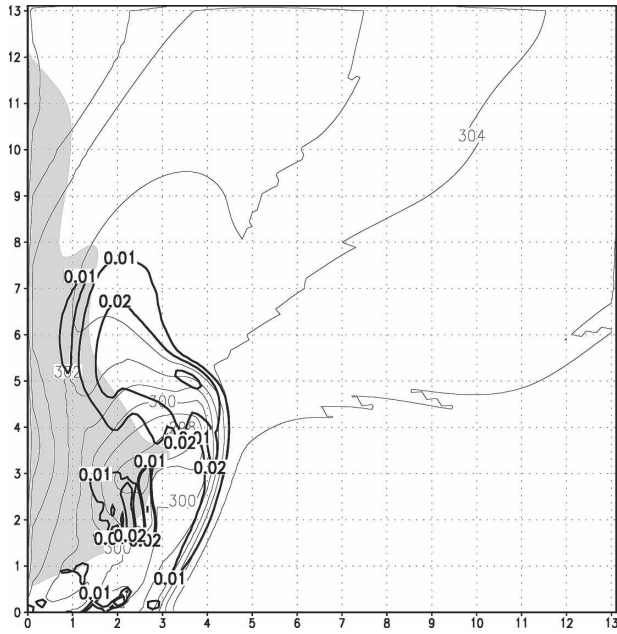


FIG. 20. Same as in Fig. 18, but for 1263 m above the surface. The maximum vertical vorticity is 0.07 s^{-1} .

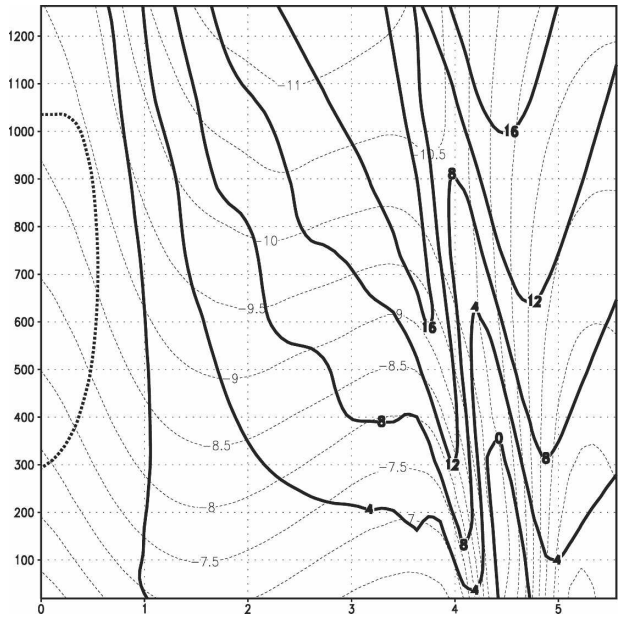


FIG. 22. Same as in Fig. 17, but taken through the vorticity maximum in Fig. 19. Potential temperature contours have been omitted for clarity.

the gust front into the cold pool. The vorticity structure shows some resemblance with that of the nonlinear pooling of vorticity in a two-dimensional barotropic framework (Guinn and Schubert 1993), where vorticity is seen to concentrate into discrete centers that are con-

nected by spiraling filaments. The maximum surface vorticity on grid 2 is 0.3 s^{-1} , which is comparable to values found in past idealized tornadic simulations with grid spacings near 100 m (Wicker and Wilhelmson 1995; Grasso and Cotton 1995). However, 100-m grid spacing is still too coarse to represent all but the largest

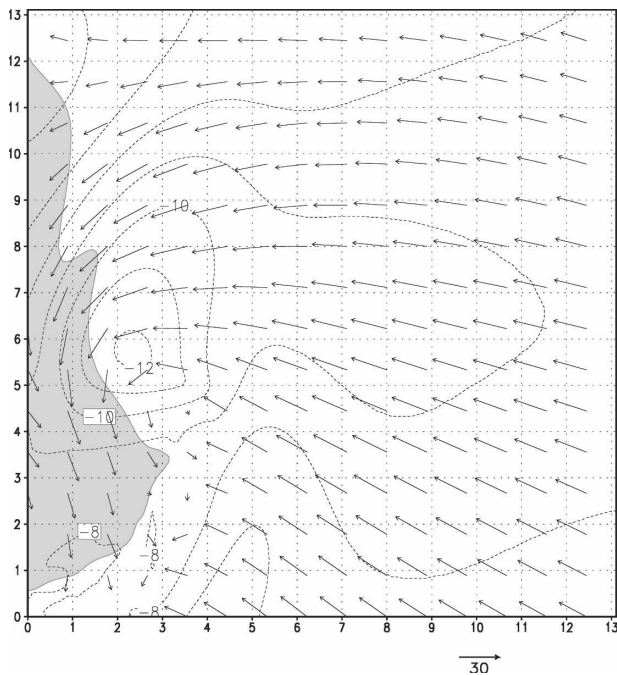


FIG. 21. Same as in Fig. 19, but for 1263 m above the surface. The minimum perturbation pressure is -12 mb .

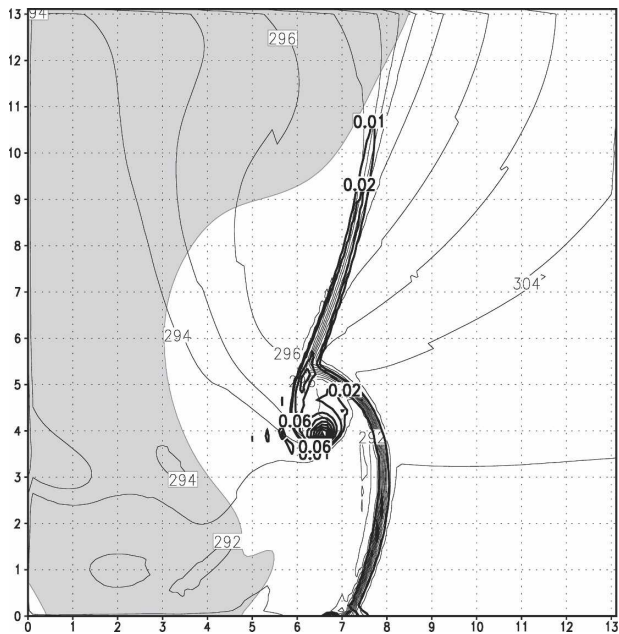


FIG. 23. Same as in Fig. 8, but at 3600 s. The maximum vertical vorticity is 0.32 s^{-1} .

tornadoes. The vortex-relative tangential wind velocities are only 25 m s^{-1} (Fig. 24), although the grid-relative velocities approach 50 m s^{-1} on the southwest side of the vortex. There is now a 12-mb pressure difference between the center of the vortex and the neighboring flow (Fig. 25), and a 7-mb difference between the vortex center and the 200-m radius of the 0.1 s^{-1} vorticity region. The relationship between the total pressure deficit of a vortex and its maximum tangential wind velocity can be written as $\Delta p_{\text{tot}}/\rho_0 = v_{\text{max}}^2/\beta$ where sample values of β are unity for a Rankine vortex, and ≈ 0.59 for the Burgers–Rott Gaussian vortex (Fiedler and Rotunno 1986). Using $v_{\text{max}} = 25 \text{ m s}^{-1}$ and $\rho_0 = 1.1 \text{ kg m}^{-3}$, we obtain a total pressure deficit of 7 mb for the Rankine vortex and 12 mb for the Burgers–Rott vortex.

At the 1263-m level (Fig. 26), there is also a concentrated vorticity center at this time, although it is located due west of the 19-m vorticity maximum, and has less than half the magnitude (0.14 s^{-1}). Nonetheless, there is a strong pressure minimum at this level as well, with an identical value to that at the surface (Fig. 27). In contrast to earlier times, the largest pressure deficit is nearly collocated with the vorticity maximum, although analysis reveals that the maximum pressure deficit is displaced slightly toward the low-level maximum vorticity. The low pressure feature at previous times is still visible to the northwest, but is clearly distinct.

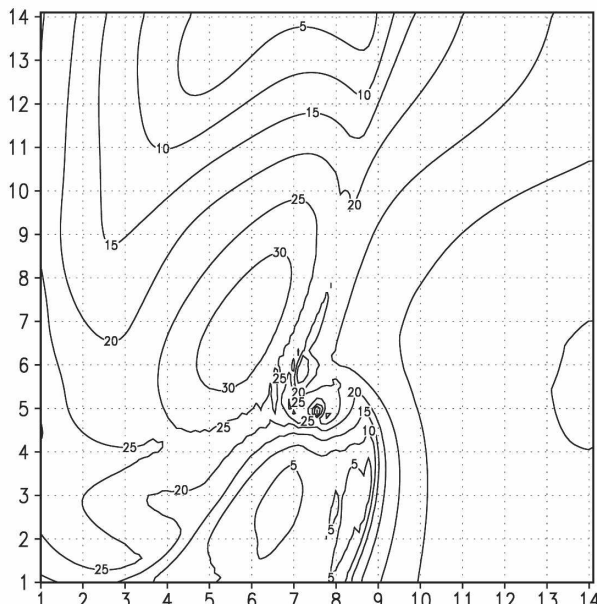


FIG. 24. The vortex-relative speed at 3600 s on grid 2. The vortex translational velocity is assumed to be $u = 19 \text{ m s}^{-1}$, $v = -6 \text{ m s}^{-1}$, based on average velocity along radius of the maximum winds.

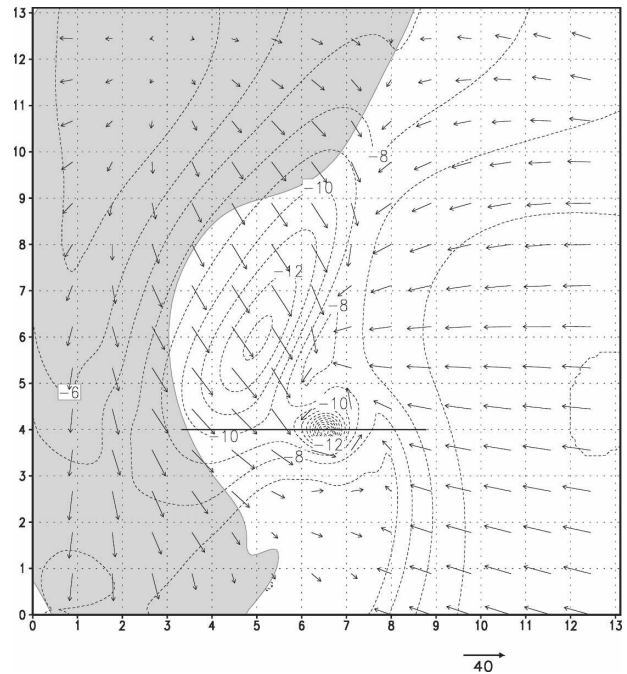


FIG. 25. Same as in Fig. 9, but at 3600 s. The minimum perturbation pressure is -19 mb . The solid line indicates the cross section in Fig. 28.

A cross section through this level (Fig. 28) is dominated by the pressure tube of the vortex. Updraft has been totally suppressed from its ambient value within the vortex. A strong downdraft appears, but only on the

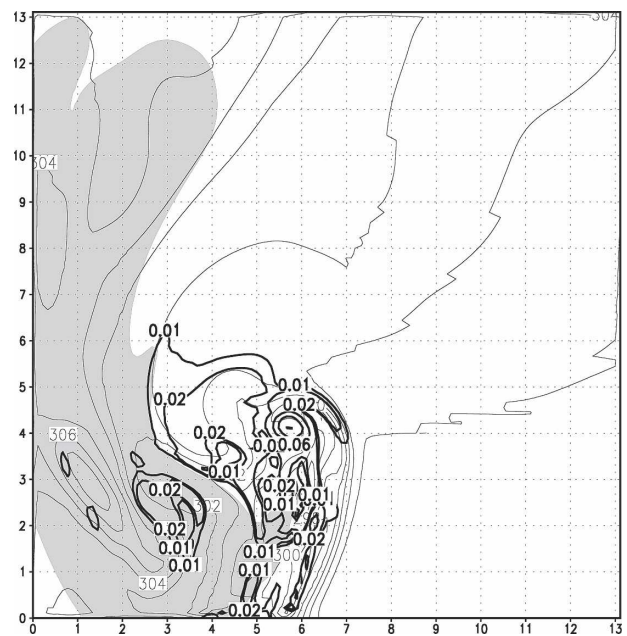


FIG. 26. Same as in Fig. 20, but at 3600 s. The maximum vertical vorticity is 0.14 s^{-1} .

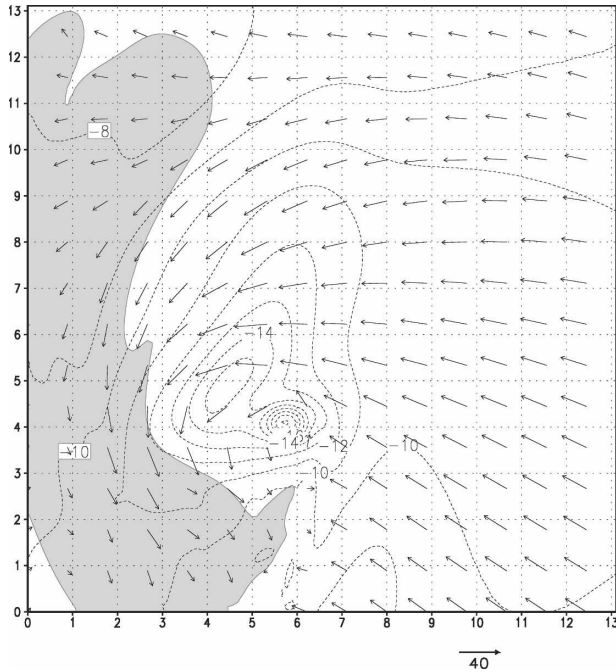


FIG. 27. Same as in Fig. 20, but at 3600 s. The minimum perturbation pressure is -19 mb.

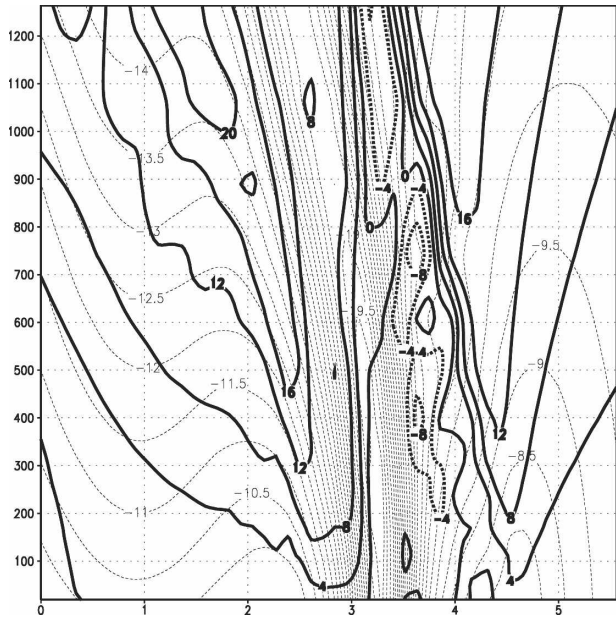
east side of the vortex. Meanwhile, a strong updraft appears near the surface on the west side (and was apparent earlier). These are due to the tilt of the vortex with height, and will be discussed more in the next

section. A plot of vertical velocity at this level (Fig. 29) shows that the downdraft is a counterclockwise intrusion into the warm sector, and resembles the occlusion downdraft of previous modeling studies (Klemp and Rotunno 1983; Wicker and Wilhelmson 1995; Adlerman et al. 1999). The enhanced updraft is a similar incursion into the cool sector.

5. Dynamic analysis

We now examine the magnitudes of the various terms in (5) and (6), keeping in mind, since RAMS is not anelastic, that W and D need not be equal, nor need the neutral terms, NV and NH , be equal. We examine the fourth model level above the surface (168 m) because closer to the surface the lower boundary conditions on the vertical momentum equation begins to become significant. Qualitatively, the model fields at this level closely resemble those at the surface (Fig. 30). We focus on the location of the maximum vertical vorticity at 3300, 3360, and 3420 s. Figure 31 compares the magnitudes of the terms V , PV , NV , and $W = V - PV - NV$ in (5), while Fig. 32 compares H , PH , NH , and $D = H + PH + NH$. Figure 33 directly compares D with W .

With regard to these graphs we note the following: 1) the dominant term, especially at later times, is H , and it is strongly negative, consistent with a decreasing pressure; 2) heuristically consistent with the decreasing pressure, the horizontal Laplacian (PH) increases



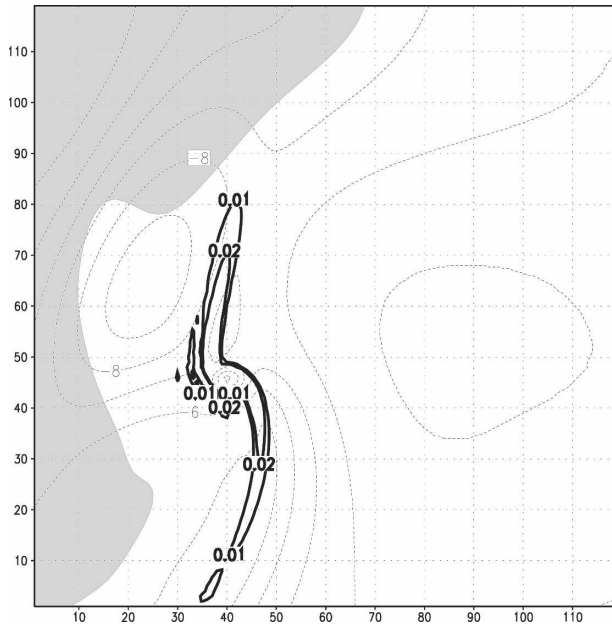


FIG. 30. Same as in Fig. 19, but for 168 m above the surface. Thick contours show the vertical vorticity values of 0.01 and 0.02 s^{-1} . The minimum perturbation pressure is -10 mb.

sharply with time; 3) PH, however, never quite counteracts H, implying that the horizontal convergence tendency is decreasing; 4) though W and D become significantly different at 3420 s, both are negative, and become increasingly so in time; 5) the decrease that does occur in W is largely attributable to an increase in PV; and 6) since this increase is not enough to equate W with D , we must conclude that the pressure will continue to decrease after 3420 s, despite the increasingly

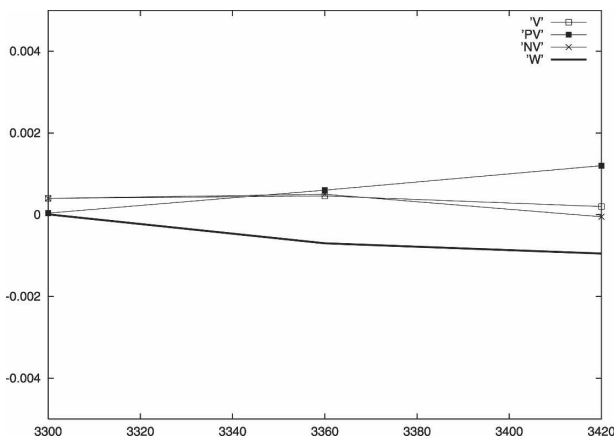


FIG. 31. The magnitude of vertical forcing term V , vertical pressure Laplacian term PV , term NV , and $W = V - PV - NV$ in (5) vs time, for the location of maximum vertical vorticity on grid 2 at 168 m above the surface. Units are s^{-2} .

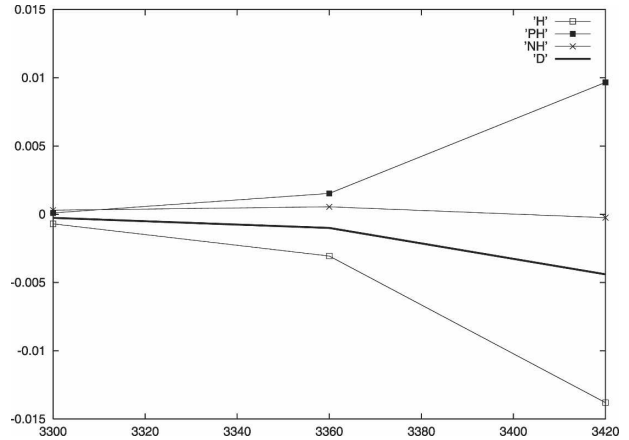


FIG. 32. Same as in Fig. 31, but for the horizontal forcing term H , horizontal pressure Laplacian term PH , term NH , and $D = H + PH + NH$ in (6) vs time.

negative horizontal convergence tendency, until either PV becomes larger, or PH nearly balances H, thus, decreasing the magnitude of D . The pressure continues to decrease until 3600 s. All of these aspects are consistent with the horizontally forced surface vortex model. Table 2 shows these terms averaged over a square centered at the maximum vorticity, and also confirms that the average horizontal convergence is indeed decreasing during vortex intensification.

How can the vortex not only survive but strengthen as the horizontal convergence decreases? As the vortex intensifies and occludes, the spatial distribution of the convergence forcing terms becomes more complicated, and advection must be taken into account. Table 3 shows the terms in Figs. 31–32 at 3480 s, but also includes the advection of horizontal convergence, as well as horizontal convergence itself. We see that at this

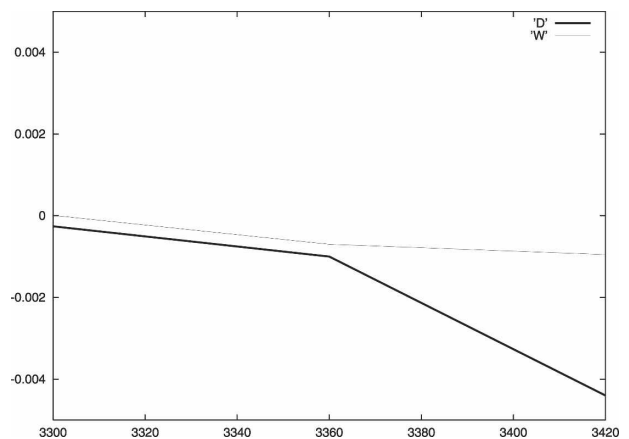


FIG. 33. Same as in Fig. 31, but for W and D terms in (5) and (6) vs time.

TABLE 2. Magnitude of horizontal divergence and terms in (5)–(6), averaged over square of side 555.56 m. The center of the square is at the location of maximum vertical vorticity on grid 2 at 168 m above the surface. Units of terms are 10^{-6} s^{-2} .

Time	V	PV	N	H	PH	Divergence (s^{-1})
3300 s	366	60	-387	-463	-16	-2.01×10^{-2}
3360 s	415	-330	-473	-1406	755	-1.90×10^{-2}
3420 s	314	-632	-441	-3849	3172	-1.33×10^{-2}
3480 s	110	-1043	34	-5566	5369	4.4×10^{-3}
3600 s	256	-1662	241	-11 052	10 835	-5.7×10^{-3}

time and location advection is an important positive contributor to an otherwise nearly balanced convergence budget. We also see that the horizontal convergence is still quite strong. But one grid point to the north, horizontal convergence is nearly absent. Though the net terms W and D are quite similar at the two locations, the advection contribution is here negative. What this shows is that while horizontal convergence may decrease on the large scale, local regions of convergence can persist, and through advection help maintain the mature vortex.

So what is the local source of horizontal convergence underlying the strong horizontal convergence advection in the mature vortex? We present figures showing the vortex at 3600 s to help answer this question. Basically, we believe that the new convergence is due to the tilt of the vortex with height, and that the interaction of the tilt with advection also accounts for the displacement of the occlusion downdraft away from the vortex, as proposed in Wakimoto et al. (1998) and Wakimoto and Cai (2000). For the mature vortex, with a mainly westward tilt with height, the dominant vertical pressure gradient forces are upward on the west side of the vortex, and downward on the east side (Fig. 34). However, rotation around the vortex aloft imparts southerly momentum to parcels in the downward pressure gradient force, and as these parcels descend they should continue to wrap around the vortex at lower levels. Thus, minima in w are displaced counterclockwise from minima in dw/dt (Fig. 35), and the downdraft at any level is displaced from the location of the lower-level vortex, allowing it to persist. Similarly, parcels in the upward pressure gra-

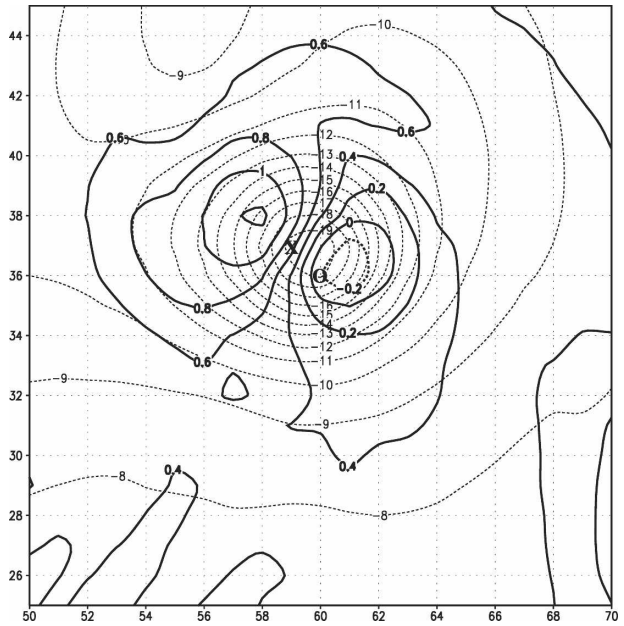


FIG. 34. Close-up of vortex at 168 m above the surface and 3600 s. Thin contours are perturbation pressure in Pa (0.01 mb). Thick contours are vertical pressure gradient force (in m s^{-2}).

dient force possess northerly momentum, and wrap counterclockwise as they ascend, leading to the displaced w maximum. This is crucial near the surface, where the $dw/dt = 0$ boundary condition dictates horizontal divergence beneath downdrafts, and the eventual dissipation of any vorticity beneath. Table 4 confirms that at 168 m both horizontal convergence and its advection are very strong one grid point southwest of the vortex center.

6. Discussion

As might be expected, the vortex evolution here defies easy and simple classification into conceptual schemes such as Figs. 2 and 3, and the compressibility (and implicit scheme) of the numerical model complicate dynamic analysis. We can make a few observations, however. It seems clear that the dominant influence on pressure reduction (and hence vortex initiation) is the horizontal term H . To the extent that there

TABLE 3. The magnitude of horizontal divergence, terms in (5)–(6), and total convergence advection (ADV). Positive ADV implies that advection is increasing horizontal convergence. Locations are those of maximum vertical vorticity on grid 2 at (top row) 168 m above the surface, and (bottom row) one grid point northward. Units of terms are 10^{-6} s^{-2} .

Grid location	V	PV	N	H	PH	ADV	Divergence (s^{-1})
(47, 42)	146	-851	1571	-27 217	29 000	3078	-2.5×10^{-2}
(47, 43)	170	-1256	1555	-15 634	18 307	-956	-4.5×10^{-3}

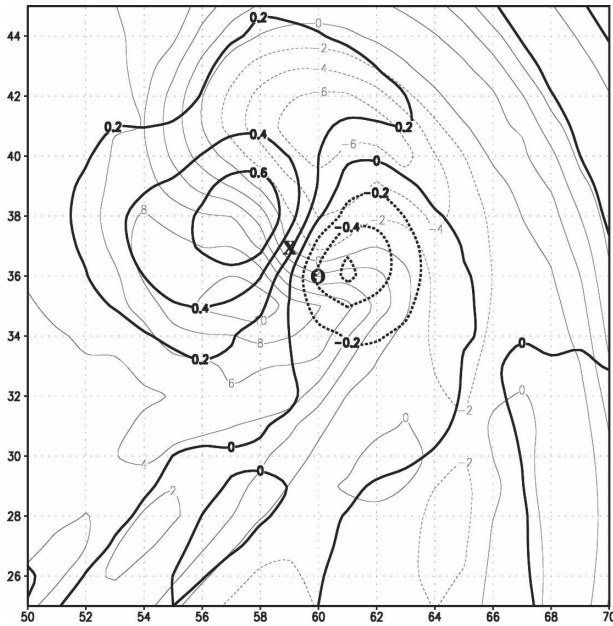


FIG. 35. Same as in Fig. 34, but thin contours are vertical velocity in m s^{-1} ; thick contours are dw/dt in m s^{-2} .

is vertical acceleration, it is generally downward, associated with the occlusion downdraft. The only upward vertical forcing that plays a direct role appears to be that associated with the tilt of the mature vortex. Lifting beneath the vortex aloft may help create horizontal convergence to maintain the mature vortex despite the occlusion downdraft. This is a complicated process where the advection and neutral (N) terms are also significant. However, vortex concentration itself occurs without any surge in horizontal convergence or vertical acceleration.

It may be argued that in an actual tornado, vertical coupling must be present because the parent storm is the only possible source of the energy needed. Indeed, one reason why the vortex here is weaker than those of Wicker and Wilhelmson (1995) and Grasso and Cotton (1995) could be that strong cloud-base updrafts were present in those studies, but not here. This upward forcing could enhance that present along the cold pool boundary. So actual tornadogenesis likely requires both horizontal and vertical forcing. However, even with additional vertical forcing in our simulation, vortex for-

mation itself should still be controlled by horizontal advective processes. The reason is that axisymmetric horizontal convergence would need to compress the vorticity band along its long axis, which takes considerable time. Horizontal advective processes, however, can induce wavelike instability along the vorticity band, and enable the formation of localized vortices. Tornadogenesis would likewise be expected to be triggered by horizontal advective processes if the source vorticity is extended in one dimension.

We do wish to fully acknowledge the ideal and simplified character of this simulation. Diffusive and surface friction effects are not addressed here. A detailed description of the structure of the vortex must include the effects of surface drag, as previously stated. Past idealized simulations of the supercell and low-level mesocyclone have traditionally been free slip, because of the relatively coarse vertical model resolution, and because of the difficulty of maintaining the circulation against existing model formulations of surface drag (Wicker and Wilhelmson 1995; Adlerman and Droege-meier 2002). In this simulation the horizontal model grid spacing is still too coarse to resolve a true tornadic vortex. Though the vortex here could produce high F1 damage on the Fujita scale (Grazulis 1993), it would be interesting to investigate if the nearby presence of vertical buoyant forcing could transmit the full energy of the thunderstorm to these vortices.

7. Conclusions

We have succeeded in modeling the formation of a concentrated vortex from a broader vorticity patch along the thermal boundary of a supercell, and have examined its formation in detail. In contrast to axisymmetric models that rely on the generation of horizontal convergence to concentrate vorticity into a strong vortex, the current vortex forms in an environment with nonaxisymmetric horizontal convergence, and is concentrated through local horizontal advective rearrangement of vorticity. A decrease of central pressure is the consequence of the vortex formation, explainable by the anelastic relation, rather than its cause. Also, the formation of the vortex is associated with a generally negative horizontal convergence tendency, although

TABLE 4. Same as in Table 3, but at 3600 s. Locations are those of the maximum vertical vorticity on grid 2 at (top row) 168 m above the surface and (bottom row) one grid point to the southwest.

Grid location	V	PV	N	H	PH	ADV	Divergence (s^{-1})
(59, 35)	194	-2446	1134	-35 723	36 290	-964	-1.2×10^{-2}
(60, 36)	251	-2511	-770	-10 774	9235	5209	-3.8×10^{-2}

the tilt of the mature vortex produces local regions of upward dynamic forcing and horizontal convergence. Advection helps to maintain the mature vortex against dissipation for a time. The evolution resembles the third tornadogenesis stage of Rotunno (1986).

We still have not explained exactly why vorticity concentrates only in a localized region of the extended vorticity band. Part II will examine this process in more detail. We will examine models of the evolution of vorticity bands residing in the axis of dilatation of plane convergence. We will show how plane convergence and shear instability can combine to produce a localized, concentrated, isolated vortex. We will also show how tangential velocities can be enhanced by this process, although not enough to fully account for observed tornadic speeds.

Acknowledgments. This research was supported by the National Science Foundation under Grant ATM-990929. The advice and assistance of Louie Grasso, Bob Walko, and Lou Wicker are acknowledged. During the completion of this manuscript the first author (BJG) held a National Research Council Research Associateship Award at the Naval Research Laboratory in Monterey, California. The comments of Paul Markowski and an anonymous reviewer greatly improved the manuscript.

APPENDIX

The Poisson Equation in *x*-*y* Rotation-Invariant Form

The incompressible inviscid π' Poisson equation is given by (e.g., Rotunno and Klemp 1982)

$$\begin{aligned} \frac{d}{dt}(\nabla \cdot \mathbf{v}) = & -\nabla \cdot (\theta_{v0} \nabla \pi') - \left(\frac{\partial u}{\partial x}\right)^2 - \left(\frac{\partial v}{\partial y}\right)^2 - \left(\frac{\partial w}{\partial z}\right)^2 \\ & - 2 \left[\frac{\partial v}{\partial x} \frac{\partial u}{\partial y} + \frac{\partial w}{\partial x} \frac{\partial u}{\partial z} + \frac{\partial w}{\partial y} \frac{\partial v}{\partial z} \right] + \frac{\partial B}{\partial z}. \end{aligned} \tag{A1}$$

Consider the *u* and *v* terms in (A1):

$$\text{horiz. terms} = - \left(\frac{\partial u}{\partial x}\right)^2 - \left(\frac{\partial v}{\partial y}\right)^2 - 2 \frac{\partial v}{\partial x} \frac{\partial u}{\partial y}, \tag{A2}$$

which are derived from the divergence of the horizontal momentum equations. Using the definitions $\zeta_z = (\partial v/\partial x - \partial u/\partial y)$, $H = (\partial v/\partial x + \partial u/\partial y)$, $\mathcal{T} = (\partial u/\partial x - \partial v/\partial y)$, and $\delta = (\partial u/\partial x + \partial v/\partial y)$, we can rewrite each term in (A2) as

$$\begin{aligned} \text{horiz. terms} = & - \left(\frac{\delta + \mathcal{T}}{2}\right)^2 - \left(\frac{\delta + \mathcal{T}}{2}\right)^2 \\ & - 2 \left(\frac{H - \zeta_z}{2}\right) \left(\frac{H + \zeta_z}{2}\right), \end{aligned} \tag{A3}$$

or

$$\begin{aligned} \text{horiz. terms} = & - \frac{2\delta^2 + 2\mathcal{T}^2 + 2H^2 - 2\zeta_z^2}{4} \\ = & - \frac{\delta^2 + \mathcal{T}^2 + H^2 - \zeta_z^2}{2}. \end{aligned} \tag{A4}$$

The quantity $\mathcal{T}^2 + H^2$ is the square of the deformation, \mathcal{D}^2 . Since δ , ζ_z , and the quantities involving vectors are all invariant to rotation in the *x*-*y* plane, so must be \mathcal{D}^2 .

Finally, if the fluid is incompressible, then the term $-(\partial w/\partial z)^2$ must be equivalent to δ^2 . Combining this term with the two-dimensional terms in (A1) yields

$$\begin{aligned} \frac{d}{dt}(\nabla \cdot \mathbf{v}) = & -\nabla \cdot (\theta_{v0} \nabla \pi') + \frac{\zeta_z^2 - 3\delta^2 - \mathcal{D}^2}{2} \\ & - 2 \left(\nabla_{HW} \cdot \frac{\partial \mathbf{v}_H}{\partial z} \right) + \frac{\partial B}{\partial z}. \end{aligned} \tag{A5}$$

REFERENCES

Adlerman, E. J., and K. K. Droegemeier, 2002: The sensitivity of numerically simulated cyclic mesocyclogenesis to variations in physical and computational parameters. *Mon. Wea. Rev.*, **130**, 2671–2691.

—, —, and R. Davies-Jones, 1999: A numerical simulation of cyclic mesocyclogenesis. *J. Atmos. Sci.*, **56**, 2045–2069.

Arakawa, A., and V. R. Lamb, 1981: A potential enstrophy and energy conserving scheme for the shallow water equations. *Mon. Wea. Rev.*, **109**, 18–36.

Atkins, N. T., M. L. Weisman, and L. J. Wicker, 1999: The influence of preexisting boundaries on supercell evolution. *Mon. Wea. Rev.*, **127**, 2910–2927.

Barnes, S. L., 1970: Some aspects of a severe, right-moving thunderstorm deduced from mesonet network rawinsonde observations. *J. Atmos. Sci.*, **27**, 634–648.

—, 1978: Oklahoma thunderstorms on 29–30 April 1970. Part I: Morphology of a tornadic storm. *Mon. Wea. Rev.*, **106**, 673–684.

Batchelor, G. K., 1967: *An Introduction to Fluid Mechanics*. Cambridge University Press, 516 pp.

Blanchard, D. O., and J. M. Straka, 1998: Some possible mechanisms for tornadogenesis failure in a supercell. Preprints, *19th Conf. on Severe Local Storms*, Minneapolis, MN, Amer. Meteor. Soc., 116–119.

Brandes, E. A., 1978: Mesocyclone evolution and tornadogenesis: Some observations. *Mon. Wea. Rev.*, **106**, 995–1011.

—, R. P. Davies-Jones, and B. C. Johnson, 1988: Streamwise vorticity effects on supercell morphology and persistence. *J. Atmos. Sci.*, **45**, 947–963.

Brooks, H. E., C. A. Doswell III, and R. P. Davies-Jones, 1993: Environmental helicity and the maintenance and evolution of

- low-level mesocyclones. *The Tornado: Its Structure, Dynamics, Prediction, and Hazards, Meteor. Monogr.*, No. 79, Amer. Meteor. Soc., 97–104.
- Browning, K. A., 1964: Airflow and precipitation trajectories within severe local storms which travel to the right of the winds. *J. Atmos. Sci.*, **21**, 634–639.
- , and F. H. Ludlam, 1962: Airflow in convective storms. *Quart. J. Roy. Meteor. Soc.*, **88**, 117–135.
- Clark, T. L., and R. D. Farley, 1984: Severe downslope windstorm calculations in two and three spatial dimensions using anelastic interactive grid nesting: A possible mechanism for gustiness. *J. Atmos. Sci.*, **41**, 329–350.
- Corcos, G. M., and F. S. Sherman, 1984: The mixing layer: Deterministic models of a turbulent flow. Part I: Introduction and the two-dimensional flow. *J. Fluid Mech.*, **139**, 29–65.
- Cotton, W. R., and R. A. Anthes, 1989: *Storm and Cloud Dynamics*. Academic Press, 883 pp.
- , and Coauthors, 2003: RAMS 2001: Current status and future directions. *Meteor. Atmos. Phys.*, **82**, 5–29.
- Davies-Jones, R. P., 1982: Observational and theoretical aspects of tomadogenesis. *Topics in Atmospheric and Oceanographic Sciences: Intense Atmospheric Vortices*, L. Bengtsson and J. Lighthill, Eds., Springer-Verlag, 175–189.
- , 1984: Streamwise vorticity: The origin of updraft rotation in supercell storms. *J. Atmos. Sci.*, **41**, 2991–3006.
- , 2002: Linear and nonlinear propagation of supercell storms. *J. Atmos. Sci.*, **59**, 3178–3205.
- , and H. E. Brooks, 1993: Mesocyclogenesis from a theoretical perspective. *The Tornado: Its Structure, Dynamics, Prediction, and Hazards, Meteor. Monogr.*, No. 79, Amer. Meteor. Soc., 105–114.
- Doswell, C. A., and D. W. Burgess, 1993: Tornadoes and tornadic storms: A review of conceptual models. *The Tornado: Its Structure, Dynamics, Prediction, and Hazards, Meteor. Monogr.*, No. 79, Amer. Meteor. Soc., 161–172.
- Fiedler, B. H., 1994: The thermodynamic speed limit and its violation in axisymmetric numerical simulations of tornado-like vortices. *Atmos.–Ocean*, **32**, 335–359.
- , 1998: Wind-speed limits in numerically simulated tornadoes with suction vortices. *Quart. J. Roy. Meteor. Soc.*, **124**, 2377–2392.
- , and R. Rotunno, 1986: A theory for the maximum wind-speeds in tornado-like vortices. *J. Atmos. Sci.*, **43**, 2328–2340.
- Finley, C. A., 1997: Numerical simulation of intense multi-scale vortices generated by supercell thunderstorms. Ph.D. dissertation, Colorado State University, 297 pp.
- Gal-Chen, T., and R. C. J. Somerville, 1975: On the use of a coordinate transformation for the solution of the Navier-Stokes equations. *J. Comput. Phys.*, **17**, 209–228.
- Gilmore, M. S., and L. J. Wicker, 2002: Influences of the local environment on supercell cloud-to-ground lightning, radar characteristics, and severe weather on 2 June 1995. *Mon. Wea. Rev.*, **130**, 2349–2372.
- Grasso, L. D., 1996: Numerical simulation of the May 15 and April 26, 1991 tornadic thunderstorms. Ph.D. dissertation, Colorado State University, 151 pp.
- , 2000: The dissipation of a left-moving cell in a severe storm environment. *Mon. Wea. Rev.*, **128**, 2797–2815.
- , and W. R. Cotton, 1995: Numerical simulation of a tornado vortex. *J. Atmos. Sci.*, **52**, 1192–1203.
- Grazulis, T. D., 1993: *Significant Tornadoes 1680–1991: A Chronology and Analysis of Events*. The Tornado Project of Environmental Films, 1326 pp.
- Guinn, T. A., and W. H. Schubert, 1993: Hurricane spiral bands. *J. Atmos. Sci.*, **50**, 3380–3403.
- Hill, G. E., 1974: Factors controlling the size and spacing of cumulus clouds as revealed by numerical experiments. *J. Atmos. Sci.*, **31**, 646–673.
- Howells, P. C., R. Rotunno, and R. K. Smith, 1988: A comparative study of atmospheric and laboratory analogue numerical tornado-vortex models. *Quart. J. Roy. Meteor. Soc.*, **114**, 801–822.
- Kessler, E., 1970: Tornadoes. *Bull. Amer. Meteor. Soc.*, **51**, 926–936.
- Klemp, J. B., and R. B. Wilhelmson, 1978a: The simulation of three-dimensional convective storm dynamics. *J. Atmos. Sci.*, **35**, 1070–1096.
- , and —, 1978b: Simulations of right- and left-moving storms produced through storm splitting. *J. Atmos. Sci.*, **35**, 1097–1110.
- , and R. Rotunno, 1983: A study of the tornadic region within a supercell thunderstorm. *J. Atmos. Sci.*, **40**, 359–377.
- Kossin, J. P., and W. H. Schubert, 2001: Mesovortices, polygonal flow patterns, and rapid pressure falls in hurricane-like vortices. *J. Atmos. Sci.*, **58**, 2196–2209.
- Lee, B. D., and R. B. Wilhelmson, 1997a: The numerical simulation of nonsupercell tornadogenesis. Part I: Initiation and evolution of pre-tornadic mesocyclone circulations along a dry outflow boundary. *J. Atmos. Sci.*, **54**, 32–60.
- , and —, 1997b: The numerical simulation of nonsupercell tornadogenesis. Part II: Evolution of a family of tornadoes along a weak outflow boundary. *J. Atmos. Sci.*, **54**, 2387–2415.
- Lemon, L. R., and C. A. Doswell III, 1979: Severe thunderstorm evolution and mesocyclone structure as related to tornadogenesis. *Mon. Wea. Rev.*, **107**, 1184–1197.
- Leslie, L. M., 1971: The development of concentrated vortices: A numerical study. *J. Fluid Mech.*, **48**, 1–21.
- Lewellen, W. S., D. C. Lewellen, and R. I. Sykes, 1997: Large-eddy simulation of a tornado's interaction with the surface. *J. Atmos. Sci.*, **54**, 581–605.
- Lilly, D. K., 1962: On the numerical simulation of buoyant convection. *Tellus*, **14**, 148–172.
- , 1969: Tornado dynamics. NCAR Manuscript 69-117, 52 pp.
- Markowski, P. M., 2002: Hook echoes and rear-flank downdrafts: A review. *Mon. Wea. Rev.*, **130**, 852–876.
- , E. N. Rasmussen, and J. M. Straka, 1998a: The occurrence of tornadoes in supercells interacting with boundaries during VORTEX-95. *Wea. Forecasting*, **13**, 852–859.
- , J. M. Straka, and E. N. Rasmussen, 1998b: A preliminary investigation of the importance of helicity “location” in the hodograph. Preprints, *19th Conf. on Severe Local Storms*, Minneapolis, MN, Amer. Meteor. Soc., 230–233.
- , —, and —, 2002: Direct surface thermodynamic observations within the rear-flank downdrafts of nontornadic and tornadic supercells. *Mon. Wea. Rev.*, **130**, 1692–1721.
- , —, and —, 2003: Tornadogenesis resulting from the transport of circulation by a downdraft: Idealized numerical simulations. *J. Atmos. Sci.*, **60**, 795–823.
- McWilliams, J. C., 1984: The emergence of isolated coherent vortices in turbulent flow. *J. Fluid Mech.*, **146**, 21–43.
- Montgomery, M. T., and R. Kallenbach, 1997: A theory for vortex Rossby waves and its application to spiral bands and intensity changes in hurricanes. *Quart. J. Roy. Meteor. Soc.*, **123**, 435–465.
- Nolan, D. S., and B. F. Farrell, 1999: The structure and dynamics of tornado-like vortices. *J. Atmos. Sci.*, **56**, 2908–2936.

- Pielke, R. A., and Coauthors, 1992: A comprehensive meteorological modeling system—RAMS. *Meteor. Atmos. Phys.*, **49**, 69–91.
- Rasmussen, E. N., and J. M. Straka, 1996: Mobile mesonet observations of tornadoes during VORTEX-95. Preprints, *18th Conf. on Severe Local Storms*, San Francisco, CA, Amer. Meteor. Soc., 1–5.
- , and D. O. Blanchard, 1998: A baseline climatology of sounding-derived supercell and tornado forecast parameters. *Wea. Forecasting*, **13**, 1148–1164.
- , J. M. Straka, R. Davies-Jones, C. A. Doswell III, F. H. Carr, M. D. Eilts, and M. D. MacGorman, 1994: Verification of the origins of rotation in tornadoes experiment: VORTEX. *Bull. Amer. Meteor. Soc.*, **75**, 995–1006.
- , S. Richardson, J. M. Straka, P. M. Markowski, and D. O. Blanchard, 2000: The association of significant tornadoes with a baroclinic boundary on 2 June 1995. *Mon. Wea. Rev.*, **128**, 174–191.
- Ray, P. S., B. C. Johnson, K. W. Johnson, J. S. Bradberry, J. J. Stephens, K. K. Wagner, R. B. Wilhelmson, and J. B. Klemp, 1981: The morphology of several tornadic storms on 20 May 1977. *J. Atmos. Sci.*, **38**, 1643–1663.
- Ritchie, E. A., and G. J. Holland, 1993: On the interaction of tropical-cyclone-scale vortices. II: Discrete vortex patches. *Quart. J. Roy. Meteor. Soc.*, **119**, 1363–1379.
- Rosenhead, L., 1931: The formation of vortices from a surface of discontinuity. *Proc. Roy. Soc. London*, **A134**, 170–192.
- Rotunno, R., 1979: A study in tornado-like vortex dynamics. *J. Atmos. Sci.*, **36**, 140–155.
- , 1981: On the evolution of thunderstorm rotation. *Mon. Wea. Rev.*, **109**, 577–586.
- , 1984: An investigation of a three-dimensional asymmetric vortex. *J. Atmos. Sci.*, **41**, 283–298.
- , 1986: Tornadoes and tornadogenesis. *Mesoscale Meteorology and Forecasting*, P. S. Ray, Ed., Amer. Meteor. Soc., 414–433.
- , and J. B. Klemp, 1982: The influence of the shear-induced pressure gradient of thunderstorm motion. *Mon. Wea. Rev.*, **110**, 136–151.
- , and —, 1985: On the rotation and propagation of simulated supercell thunderstorms. *J. Atmos. Sci.*, **42**, 271–292.
- Schlesinger, R. E., 1975: A three-dimensional numerical model of an isolated deep convective cloud: Preliminary results. *J. Atmos. Sci.*, **32**, 934–957.
- Smagorinsky, J., 1963: General circulation experiments with the primitive equations. 1: The basic experiment. *Mon. Wea. Rev.*, **91**, 99–164.
- Smith, R. K., and L. M. Leslie, 1978: Tornadogenesis. *Quart. J. Roy. Meteor. Soc.*, **104**, 189–199.
- Snow, J. T., and R. L. Pauley, 1984: On the thermodynamic method for estimating maximum tornado windspeeds. *J. Climate Appl. Meteor.*, **23**, 1465–1468.
- Trapp, R. J., 1999: Observations of nontornadic low-level mesocyclones and attendant tornadogenesis failure during VORTEX. *Mon. Wea. Rev.*, **127**, 1693–1705.
- , and R. Davies-Jones, 1997: Tornadogenesis with and without a dynamic pipe effect. *J. Atmos. Sci.*, **54**, 113–133.
- , E. D. Mitchell, G. A. Tipton, D. W. Effertz, A. I. Watson, D. L. Andra Jr., and M. A. Magsig, 1999: Descending and nondescending tornadic vortex signatures detected by WSR-88Ds. *Wea. Forecasting*, **14**, 625–639.
- Tripoli, G. J., and W. R. Cotton, 1981: The use of ice-liquid water potential temperature as a thermodynamic variable in deep atmospheric models. *Mon. Wea. Rev.*, **109**, 1094–1102.
- van den Heever, S. C., and W. R. Cotton, 2004: The impact of hail size on simulated supercell storms. *J. Atmos. Sci.*, **61**, 1596–1609.
- Wakimoto, R. M., 1982: The life cycle of thunderstorm gust fronts as viewed with Doppler radar and rawinsonde data. *Mon. Wea. Rev.*, **110**, 1060–1082.
- , and C. Liu, 1998: The Garden City, Kansas, storm during VORTEX 95. Part II: The wall cloud and tornado. *Mon. Wea. Rev.*, **126**, 372–392.
- , and H. Cai, 2000: Analysis of a nontornadic storm during VORTEX 95. *Mon. Wea. Rev.*, **128**, 565–592.
- , C. Liu, and H. Cai, 1998: The Garden City, Kansas, storm during VORTEX 95. Part I: Overview of the storm's life cycle and mesocyclogenesis. *Mon. Wea. Rev.*, **126**, 372–392.
- Walko, R. L., 1993: Tornado spin-up beneath a convective cell: Required basic structure of the near-field boundary layer winds. *The Tornado: Its Structure, Dynamics, Prediction, and Hazards*, Meteor. Monogr., No. 79, Amer. Meteor. Soc., 89–95.
- , W. R. Cotton, M. P. Meyers, and J. Y. Harrington, 1995: New RAMS cloud microphysics parameterization. Part I: The single-moment scheme. *Atmos. Res.*, **38**, 29–62.
- Weisman, M. L., and J. B. Klemp, 1982: The dependence of numerically simulated convective storms on vertical wind shear and buoyancy. *Mon. Wea. Rev.*, **110**, 504–520.
- Wicker, L. J., and R. B. Wilhelmson, 1995: Simulation and analysis of tornado development and decay within a three-dimensional supercell thunderstorm. *J. Atmos. Sci.*, **52**, 2675–2703.
- Wilhelmson, R. B., and J. B. Klemp, 1981: A three-dimensional numerical simulation of splitting severe storms on 3 April 1964. *J. Atmos. Sci.*, **38**, 1581–1600.
- Winant, C. D., and F. K. Browand, 1974: Vortex pairing: The mechanism of mixing layer growth at moderate Reynolds number. *J. Fluid Mech.*, **63**, 237–255.